Neuronal calcium wave propagation varies with changes in endoplasmic reticulum parameters: a computer model

Samuel A. Neymotin[1,2,+,*], **Robert A. McDougal**[2,+], **Mohamed A. Sherif**[3,4,5,6], **Christopher P. Fall**[7], **Michael L. Hines**[2], and **William W. Lytton**[1,8,9]

[1]Dept. Physiology & Pharmacology, SUNY Downstate, 450 Clarkson Avenue, Brooklyn, NY, 11203

[2]Dept. Neurobiology, Yale University School of Medicine, 333 Cedar St. New Haven, CT 06510

[3]Dept. Psychiatry and Behavioral Sciences, SUNY Downstate, 450 Clarkson Avenue, Brooklyn, NY, 11203

[4]Program in Biomedical Engineering, SUNY Downstate / NYU-Poly, Brooklyn, NY, 11203

[5]Dept. Neuropsychiatry, Ain Shams University School of Medicine, Cairo, Egypt

[6]Dept. Psychiatry, Yale University School of Medicine, VA Connecticut Healthcare System, West Haven, CT, 06516

[7]Dept. Computer Science, Georgetown University, Washington D.C. 20057

[8]Dept. Neurology, SUNY Downstate, 450 Clarkson Avenue, Brooklyn, NY, 11203

[9]Kings County Hospital, Brooklyn, NY, 11203

Abstract

Calcium (Ca^{2+}) waves provide a complement to neuronal electrical signaling, forming a key part of a neuron's second messenger system. We developed a reaction-diffusion model of an apical dendrite with diffusible inositol triphosphate (IP_3), diffusible Ca^{2+}, IP_3 receptors (IP_3Rs), endoplasmic reticulum (ER) Ca^{2+} leak, and ER pump (SERCA) on ER. Ca^{2+} is released from ER stores via IP_3Rs upon binding of IP_3 and Ca^{2+}. This results in Ca^{2+}-induced-Ca^{2+}-release (CICR) and increases Ca^{2+} spread. At least two modes of Ca^{2+} wave spread have been suggested: a continuous mode based on presumed relative homogeneity of ER within the cell; and a pseudo-saltatory model where Ca^{2+} regeneration occurs at discrete points with diffusion between them. We compared the effects of three patterns of hypothesized IP_3R distribution: 1. continuous homogeneous ER, 2. hotspots with increased IP_3R density (IP_3R *hotspots*), 3. areas of increased ER density (ER *stacks*). All three modes produced Ca^{2+} waves with velocities similar to those measured *in vitro* (~50–90μm /sec). Continuous ER showed high sensitivity to IP_3R density increases, with time to onset reduced and speed increased. Increases in SERCA density resulted in opposite effects. The measures were sensitive to changes in density and spacing of IP_3R hotspots and stacks. Increasing the apparent diffusion coefficient of Ca^{2+} substantially increased wave speed. An extended electrochemical model, including voltage gated calcium channels and AMPA

---
[*]corresponding author.
[+]authors contributed equally

synapses, demonstrated that membrane priming via AMPA stimulation enhances subsequent Ca^{2+} wave amplitude and duration. Our modeling suggests that pharmacological targeting of IP_3Rs and SERCA could allow modulation of Ca^{2+} wave propagation in diseases where Ca^{2+} dysregulation has been implicated.

Keywords

Calcium waves; computer model; SERCA; IP_3 receptor; reaction-diffusion; calcium; electrochemical

1 Introduction

Calcium (Ca^{2+}) is an important second messenger signal in many cell types, with diverse roles, from fertilization (Busa and Nuccitelli, 1985; Kretsinger, 1980) to regulating gene expression (West et al., 2001). Ca^{2+} is involved in triggering destructive processes including apoptosis (Orrenius et al., 2003) and ischemia (Lipton, 1999). Cells, including neurons, therefore regulate cytosolic Ca^{2+} concentration via buffers (Stern, 1992) and sequestration into mitochondria (Gunter et al., 2004) or endoplasmic reticulum (ER) (Berridge, 1998). In neurons, sequestration is modulated by neuronal activity (Pozzo-Miller et al., 1997), and elevated Ca^{2+} opens certain ion channels. There is therefore a bidirectional interaction between chemical signaling and electrophysiology (Blackwell, 2013; De Schutter and Smolen, 1998; De Schutter, 2008).

Ca^{2+} is heavily buffered but travels long distances (>100 μm) to reach its targets. This poses a temporal problem if relying purely on diffusion. Ca^{2+} waves increase the rapidity of Ca^{2+} spread via Ca^{2+}-induced-Ca^{2+}-release (CICR). CICR occurs in neurons and requires stores of Ca^{2+} held in the ER. ER is distributed throughout the cytosol in a connected way, through the dendrites and dendritic spines (Harris, 1994; Spacek and Harris, 1997). The ER SERCA pump pushes Ca^{2+} from the cytosol into the ER. When triggered by IP_3 and Ca^{2+}, the ER IP_3 receptors (IP_3Rs) open and release some of the ER's Ca^{2+} into the cytosol. Regions of elevated Ca^{2+} then spread throughout portions of the dendritic tree (Ross et al., 2005).

Understanding Ca^{2+} wave modulation is difficult since cytosolic Ca^{2+} changes over time and passes between different intracellular compartments and extracellular space (Fall et al., 2004; Wagner et al., 2004). Adding to this complexity is the nonuniform distribution of IP_3Rs, with clusters forming where local variations in IP_3R or ER is heightened (Fitzpatrick et al., 2009).

At least two modes of Ca^{2+} wave spread have been identified: a continuous model that depends on continuous underlying substrate of regenerative potential, and a pseudosaltatory model where Ca^{2+} regeneration occurs at discrete points with diffusion between them. (We call it pseudo-saltatory here to distinguish from classical saltatory conduction in myelinated fibers, involving capacitative effects in addition to electrodiffusion.) It has been hypothesized that these two modes produce downstream functional differences in dendrites, where many mechanisms are responsive to the level of Ca^{2+}, for example I_h (Winograd et

al., 2008; Neymotin et al., 2013, 2014) and synaptic plasticity (Kotaleski and Blackwell, 2010).

To investigate Ca^{2+} waves in a spatiotemporal context relevant for neurons, we developed a model of Ca^{2+} waves which includes cytosol and ER. Baseline cytosolic Ca^{2+} and IP_3 concentration are set to low values. The model includes ER SERCA pumps (pump Ca^{2+} from cytosol into ER), leak channels (Ca^{2+} leaks out of ER), and IP_3Rs. Our model generates Ca^{2+} waves with realistic physiological properties. We use our model to investigate how IP_3R density and clustering, alterations in SERCA density, alterations in ER stacking, and Ca^{2+} diffusibility alter waves. An additional complexity arises when we consider coupling to plasma membrane calcium channels which will contribute additional calcium flux triggered by rapidly-spreading regenerative voltage changes on the membrane. We have therefore also assessed our results in an extended electrochemical model, which included a variety of ion channels (leak, voltage-dependent calcium channels: VGCC, potassium, sodium) with synaptic activation. We used this model to demonstrate how priming due to AMPA-mediated membrane depolarization would enhance subsequent Ca^{2+} wave amplitude and duration.

2 Materials and methods

All simulations were run in the NEURON (version 7.3) simulation environment (Carnevale and Hines, 2006). NEURON has traditionally supported electrical modeling but has recently been extended to support reaction-diffusion (R×D) modeling as well (McDougal et al., 2013a,b). The full 1D R×D calcium wave model of the neuronal dendrite (depicted in Fig. 1) and the data analysis source-code is available on ModelDB (Peterson et al., 1996; Hines et al., 2004) (http://senselab.med.yale.edu/modeldb).

Our Ca^{2+} dynamics are derived from Wagner et al. (2004), a spatial variant of Li and Rinzel (1994). Parameters are as in Table 1. We modeled a one-dimensional R×D system of intracellular neuronal Ca^{2+} waves in an unbranched apical dendrite of a hippocampal pyramidal neuron (length of 1000 μm and diameter of 1 μm). Within the dendrite, we modeled cytosolic and endoplasmic reticulum (ER) compartments by using a fractional volume for each: suppose that for a given cell volume, f_{ER} denotes the fraction occupied by the ER (0.17), and f_{cyt} denotes the fraction occupied by the cytosol (0.83). Necessarily $f_{cyt} + f_{ER} \leq 1$. The inequality is strict if other structures are present, such as mitochondria.

ER-based calcium dynamics were previously modeled (De Young and Keizer, 1992). This previous work showed by a time-scale analysis that the qualitative dynamics of IP_3 receptors (IP_3Rs) could be represented by only considering the slow Ca^{2+} inactivation binding site state (Li and Rinzel, 1994). This work formed the basis of much subsequent work in intracellular Ca^{2+} dynamics (Fall and Rinzel, 2006; Fall et al., 2004; Hartsfield, 2005; Peercy, 2008; Wagner et al., 2004). The model presented here is a variant that neglects dynamic IP_3 production (Wagner et al., 2004).

The ER Ca^{2+} model involves IP_3Rs and SERCA pumps. As with the plasma membrane model, we combine the net effects of all other channels on the ER into a leak channel. We

denote by J_{IP3R}, J_{SERCA}, and J_{leakER} the mass flux per unit volume due to the IP$_3$R, SERCA pump, and leak channels, respectively. Dividing the mass flux by the volume fraction gives the change in concentration.

State Variables

Cytosolic Ca^{2+} concentration, ER Ca^{2+} concentration, IP$_3$ concentration, and IP$_3$R gating are denoted by Ca_{cyt}^{2+}, Ca_{ER}^{2+}, IP$_3$, and h_{IP3R}, respectively.

$$\frac{\partial Ca_{cyt}^{2+}}{\partial t} = d_{Ca_{cyt}^{2+}} \cdot \Delta Ca_{cyt}^{2+} + \frac{J_{IP3R} - J_{SERCA} + J_{leakER}}{f_{cyt}} + c_{ionic} \quad (1)$$

$$\frac{\partial Ca_{ER}^{2+}}{\partial t} = d_{Ca_{ER}^{2+}} \cdot \Delta Ca_{ER}^{2+} - \frac{J_{IP3R} - J_{SERCA} + J_{leakER}}{f_{ER}} \quad (2)$$

$$\frac{\partial IP_3}{\partial t} = d_{IP_3} \cdot \Delta IP_3 \quad (3)$$

$$\frac{\partial h_{IP_3R}}{\partial t} = \frac{h_{\infty IP_3R} - h_{IP_3R}}{\tau_{IP_3R}} \quad (4)$$

where c_{ionic} denotes the net flux into the cytosol due to ion channels on the cell membrane and depends on both space and time. The first terms of the right hand sides is the contribution from diffusion. IP$_3$ diffusion within the cytosol is passive. Equation (1) allows for the coupling between Ca^{2+} that enters the cytosol via the ion channels on the cell membrane and the intracellular Ca^{2+} which is shuttled into ER via SERCA pumps.

Fluxes

Flux from the IP$_3$R, SERCA pump, and leak channels are denoted by J_{IP3R}, J_{SERCA}, and J_{leakER}, respectively.

$$J_{IP3R} = \overline{p}_{IP_3R} \cdot m_{IP_3R}^3 \cdot n_{IP_3R}^3 \cdot h_{IP_3R}^3 \cdot (Ca_{ER}^{2+} - Ca_{cyt}^{2+})/\Xi \quad (5)$$

$$J_{SERCA} = -\frac{\overline{p}_{serca} \cdot Ca_{cyt}^{2+^2}}{(k_{serca}^2 + Ca_{cyt}^{2+^2}) \cdot \Xi} \quad (6)$$

$$J_{leakER} = \overline{p}_{leakER} \cdot (Ca_{ER}^{2+} - Ca_{cyt}^{2+})/\Xi \quad (7)$$

Here, $\Xi = N_A/10^{18} \approx 602214.129$, and is the number of molecules in a cubic micron at a concentration of 1 mM, where N_A is the Avogadro constant. The SERCA pump is a pump rather than a channel and so is modeled with Hill-type dynamics. The form of the fluxes J_{IP3R} and J_{leakER} parallels the forms for ion channels in the Hodgkin-Huxley equations.

Leak is ungated whereas J_{IP3R} is gated: m_{IP3R} and n_{IP3R} are fast gating variables depending on IP$_3$ and Ca^{2+}, and h_{IP3R} is the slow Ca^{2+} inactivation gating variable.

$$m_{\text{IP}_3\text{R}} = \frac{\text{IP}_3}{\text{IP}_3 + k_{\text{IP}_3}} \quad (8)$$

$$n_{\text{IP}_3\text{R}} = \frac{\text{Ca}^{2+}_{\text{cyt}}}{\text{Ca}^{2+}_{\text{cyt}} + k_{act}} \quad (9)$$

$$h_{\infty \text{IP}_3\text{R}} = \frac{k_{inh}}{k_{inh} + \text{Ca}^{2+}_{\text{cyt}}} \quad (10)$$

Initial values of Ca$^{2+}_{\text{cyt}}$, C_{AVG}, IP$_3$, and h_{IP3R} were set to 0.0001 mM, 0.0017 mM, 0.1 mM, and 0.8, respectively. Ca$^{2+}_{\text{ER}}$ was then adjusted based on the cytosolic and ER fractional volumes according to: $\text{Ca}^{2+}_{\text{ER}} = \dfrac{C_{\text{AVG}} - \text{Ca}^{2+}_{\text{cyt}} \cdot f_{cyt}}{f_{ER}}$

This model supports both bistable and excitable waves. Both types of waves have been observed in the Xenopus oocyte (Fontanilla and Nuccitelli, 1998; Lechleiter et al., 1991), although not clearly defined in neurons.

Electrical dynamics

Electrical dynamics were utilized for the subset of simulations described in the final figure. Electrical dynamics in the dendrite followed the standard parallel conductance model. Ion channels were based on a prior model of a hippocampal pyramidal cell (Safiulina et al., 2010) (http://senselab.med.yale.edu/modeldb/ShowModel.asp?model=126814) and included L-, N-, and T-type Ca^{2+} channels, which allowed extracellular calcium to enter the dendrite at different voltage levels (McCormick and Huguenard, 1992; Kay and Wong, 1987). The equations for the ion channels follow, leak, Na$^+$ and K$^+$ currents were represented by the conductance approximation: $I_{\text{ion}} = g_{\text{ion}} \cdot (V - E_{\text{ion}})$ (g conductance; E reversal potential) using $E_{Na} = 50$ mV; $E_k = -77$ mV; $E_{leak} = -64$ mV; ($g_{leak} = 39.4 \cdot 10^{-6}$ S/cm^2), while the Goldman-Hodgkin-Katz (GHK) flux equation was used for Ca^{2+} currents: $I_{\text{Ca}} = p_{\text{Ca}} \cdot \text{GHK}_{\text{Ca}}$ (p permeability). Channel dynamics were corrected for temperature by a Q$_{10}$ using the factor of $qt = Q_{10}^{(T-25)/10}$ with T=37°Celsius and 25° was taken to be the temperature at which the experiment was done. Conductances and activation curves were not corrected for temperature (Iftinca et al., 2006). Voltage sensitive channels largely followed variants on the Hodgkin-Huxley formalism, whereby $\dfrac{dx}{dt} = \dfrac{x_\infty - x}{\tau_x}$ using steady-state value: $x_\infty = \dfrac{\alpha_\infty}{\alpha_\infty + \beta_\infty}$, the τ_x forms either

$$\tau_{\text{EQN1}} : \tau_x = \frac{1}{qt \cdot (\alpha_\tau + \beta_\tau)} \text{ or } \tau_{\text{EQN2}} : \tau_x = \frac{\beta_\tau}{qt \cdot a_0 \cdot (1 + \alpha_\tau)}$$

were where x is m or n for an activation variable and h for an inactivation variable. F is Faraday's constant; R is the gas constant. Variations on this scheme are noted below.

L-type Ca^{2+} channel: $p_L = \bar{p}_L \cdot m_L^2 \cdot h_L$ with $\bar{p}_L = 10^{-6} cm/s$; h_L (inactivation) was Ca^{2+} dependent: $h_L(\text{Ca}_{cyt}^{2+}) = \dfrac{k_i}{k_i + \text{Ca}_{cyt}^{2+}}$ with $k_i = 0.001$ mM;

$m_L : \alpha_\infty = \dfrac{15.69 \cdot (-V+81.5)}{\exp((-V+81.5)/10.0) - 1.0}$; $\beta_\infty = 0.29 \cdot \exp(-V/10.86)$; τ_{EQN2} with $\alpha_\tau = \exp(0.0378 \cdot 2 \cdot (V-4))$, $\beta_\tau = \exp(0.0378 \cdot 2 \cdot 0.1 \cdot (V-4))$; $a_0 = 0.1$; $Q_{10}=5$.

T-type Ca^{2+} channel: $p_T = \bar{p}_T \cdot m_T^2 \cdot h_T$ with $\bar{p}_T = 10^{-6} cm/s$;

$m_T : \alpha_\infty = \dfrac{0.2 \cdot ((-V+19.26)}{\exp(((-V+19.26)/10.0) - 1.0)}$; $\beta_\infty = 0.009 \cdot \exp(-V/22.03)$; τ_{EQN2} with $\alpha_\tau = \exp(0.0378 \cdot 2 \cdot (V-(-28)))$; $\beta_\tau = \exp(0.0378 \cdot 2 \cdot 0.1 \cdot (V-(-28)))$; h_T: $\alpha_\infty = 10^{-6} \cdot \exp(-V/16.26)$; $\beta_\infty = \dfrac{1}{\exp((-V+29.79)/10)+1}$; τ_{EQN2} with $\alpha_\tau = \exp(0.0378 \cdot 3.5 \cdot (V-(-75)))$; $\beta_\tau = \exp(0.0378 \cdot 3.5 \cdot 0.6 \cdot (V-(-75)))$; $a_0=0.04$; $Q_{10}=5$.

N-type Ca^{2+} channel: $p_N = \bar{p}_N \cdot m_N^2 \cdot h_N \cdot h2_N$ with $\bar{p}_N = 10^{-6} cm/s$; m_N used $\alpha_\infty = 0.1967 \cdot (-V+19.88)/(\exp((-V+19.88)/10.0)-1.0)$; $\beta_\infty = 0.046 \cdot \exp(-V/20.73)$; τ_{EQN2} with $\alpha_\tau = \exp(0.0378 \cdot 2 \cdot (V-(-14)))$; $\beta_\tau = \exp(0.0378 \cdot 2 \cdot 0.1 \cdot (V-(-14)))$; h_N following: $\alpha_\infty = 1.6 \cdot 10^{-4} \cdot \exp(-V/48.4)$; $\beta_\infty = 1/(\exp((-V+39.0)/10)+1)$; constant $\tau_h = 80$; with $h2_N = \{0.001\}/\{0.001 + \text{Ca}_{cyt}^{2+}\}$; $a_0=0.03$, $Q_{10}=5$.

The model also contained: a transient sodium channel I_{Na} and a delayed rectifier channel I_{K-DR} to allow for action potential generation; a calcium-dependent potassium channel which hyperpolarized the cell after calcium influx; and an A-type potassium channel for rapid inactivation. Equations for these channels follow.

Na channel: $g_{Na} = \bar{g}_{Na} \cdot m_{Na}^3 \cdot h_{Na} \cdot s_{Na}$ with $\bar{g}_{Na} = 0.11$ S/cm^2; m_{Na} using τ_{EQN1} with: $\alpha = 0.4 \cdot (V-(-30+6))/(1-\exp(-(V-(-30+6)/7.2)))$; $\beta = 0.124 \cdot (-V-(30-6))/(1-\exp(-(V-(30-6)))/7.2)$ h_{Na} with special form $h_\infty = \dfrac{1}{1+\exp((V-(-50)-6)/4)}$ and using τ_{EQN1} with $\alpha_\tau = 0.03 \cdot (V-(-45+6))/(1-\exp(-(V-(-45+6))/1.5))$ and $\beta_\tau = 0.01 \cdot (V-(45-6))/(1-\exp(-(V-(45-6))/1.5))$; $Q_{10}=2$; s_{Na}: $s_\infty(V) = 1$; τ_{EQN2} with $\alpha_\tau = \exp(10^{-3} \cdot 12 \cdot (V+54) \cdot 9.648 \cdot 10^4/(8.315 \cdot (273.16 + T)))$ and $\beta_\tau = \exp(10^{-3} \cdot 12 \cdot 0.2 \cdot (V+54) \cdot 9.648 \cdot 10^4/(8.315 \cdot (273.16 + T)))$.

Delayed rectifier K channel: $g_{K-DR} = \bar{g}_{K-DR} \cdot n_{K-DR}$ where $\bar{g}_{K-DR} = 0.01$ S/cm^2;

n_{K-DR} following an atypical steady-state: $n_\infty = \dfrac{1}{1+\alpha}$ with $\alpha = \exp(10^{-3} \cdot -3 \cdot (V-19) \cdot 9.648 \cdot 10^4/(8.315 \cdot (273.16+T)))$ using the same α in τ_{EQN1} with $\beta = \exp(10^{-3} \cdot -3 \cdot 0.7 \cdot (V-19) \cdot 9.648 \cdot 10^4/(8.315 \cdot (273.16 + T)))$; $a_0=0.02$; $Q_{10}=1$.

BK-type Ca^{2+}dependent potassium channel (K_{Ca}): $g_{KCa} = \bar{g}_{KCa} \cdot o_{KCa}$ with $\bar{g}_{KCa} = 0.009$ S/cm^2; o_{KCa}:

$\alpha = \{0.28 \cdot \text{Ca}_{cyt}^{2+}\}/\{\text{Ca}_{cyt}^{2+} + k1 \cdot \exp(-2 \cdot 0.84 \cdot F \cdot V/R/(273.15+T)\}$;

$\beta = 0.48/\{1 + Ca_{cyt}^{2+}/k2 \cdot \exp(-2 \cdot F \cdot V/R/(273.15 + T))\}$ with $k1 = 0.48 \cdot 10^{-3}$; $k2 = 0.13 \cdot 10^{-6}$; using τ_{EQN1}.

A-type potassium channel, K_A: $g_A = \bar{g}_A \cdot n_A \cdot l_A$ where $\bar{g}_A = 0.02\ S/cm^2$; n_A with τ_{EQN2} and an atypical steady-state value: $n_\infty = \dfrac{1}{1+\alpha}$ with $\alpha = \exp(10^{-3} \cdot \zeta(V) \cdot (V - 17) \cdot 9.648 \cdot 10^4/(8.315 \cdot (273.16 + T)))$; $\beta_n(V) = \exp(10^{-3} \cdot \zeta(V) \cdot 0.55 \cdot (V - 17) \cdot 9.648 \cdot 10^4/(8.315 \cdot (273.16 + T)))$; $\zeta(V) = -1.5 + (-1/(1 + \exp((V + 34)/5)))$; $a_0 = 0.05$; $Q_{10} = 5$. l_A: with steady-state: $l_\infty = \dfrac{1}{1+\alpha}$; $\alpha = \exp(10^{-3} \cdot 3 \cdot (V + 50) \cdot 9.648 \cdot 10^4/(8.315 \cdot (273.16 + T)))$; time-constant: $\tau = 0.26 \cdot (V + 44) \cdot qt$; $Q_{10} = 1$.

Synapses

The AMPA receptor was modeled with a double-exponential mechanism: rise 0.05 ms, decay 5.3 ms, E_{AMPA} 0 mV. A single AMPA synapse was placed at 500 μm – midway on the dendrite; synaptic weight = 0.5 μS. The metabotropic synapse was not modeled in detail but was given as a local 12.5× increase in IP$_3$ (1.25 μM) in a 4 micron segment at the same location.

Simulation variations

In one set of simulations, we changed the density of IP$_3$R and SERCA, by scaling $p_{IP_3R}^-$ and p_{serca}^-, respectively. IP$_3$R hotspots were modeled by scaling $p_{IP_3R}^-$ at discrete locations, while keeping IP$_3$R density in between the hotspots at 0.8× baseline IP$_3$R density. ER stacks were simulated by scaling $p_{IP_3R}^-$, p_{serca}^-, and p_{leakER}^- simultaneously, while keeping ER density in between the stacks at 0.8× baseline density. Changes in Ca^{2+} buffering were simulated by scaling the Ca^{2+} diffusion coefficients, $d_{Ca_{cyt}^{2+}}$ and $d_{Ca_{ER}^{2+}}$, in equal amounts. We also modulated d_{IP_3} in a set of simulations. The range of parameter values examined were constrained to generate Ca^{2+} waves with wave features (onset, speed, duration, amplitude) that were around ranges for experimentally-observed limits in neurons (Nakamura et al., 1999; Ross et al., 2005; Fitzpatrick et al., 2009).

Electrochemical simulation variations

One set of simulations (Fig. 11) was run with the electrical dynamics (see **Electrical dynamics** above) to determine how AMPA-ergic stimulation's alteration of membrane potential prior to an IP$_3$ stimulus impacts the subsequent Ca^{2+} waves. Simulations were run for 12 s. Background IP$_3$ concentration in these simulations was set between 0–0.01 mM to prevent spontaneous oscillations. AMPA activations (150 spikes with interspike interval of 25 ms) finished 250 ms prior to IP$_3$ stimulus (amplitude: 2.5 mM).

Data analysis

Ca^{2+} and IP$_3$ concentrations were recorded in a 3D array using temporal and spatial resolution of 5 ms and 1 μm. Cytosolic Ca^{2+} wave features were extracted by thresholding the array using an amplitude threshold of 2× baseline cytosolic Ca^{2+} concentration (2.5× for the electrical simulations). Wave onset was defined as the delay after IP$_3$ stimulus until the

Ca^{2+} passed threshold. Amplitude was maximum Ca^{2+} concentration. Speed was calculated using onset time at stimulation location and final onset time at location of wave termination (note that use of final onset time leads to artifactual lowering of wave speed in pathological condition of multiple Ca^{2+} waves). Duration was calculated as median at each position from wave onset to offset (going below threshold).

3 Results

This study involved over 4800 15–30 second simulations, testing how variations in levels of IP$_3$R density, SERCA density, IP$_3$ hotspots, and ER stacks, altered wave initiation, amplitude, speed, and duration. An additional set of 32 twelve-second simulations were run, testing how the number of AMPA inputs prior to an IP$_3$ stimulus impacted the calcium waves. Simulations were run using the NEURON simulator on Linux on a 2.27 GHz quad-core Intel XEON CPU. Thirty seconds of simulation ran in 1.5–2 minutes, depending on simulation type.

We simulated the arrival of IP$_3$ from a metabotropic receptor activation cascade as an instantaneous augmentation of IP$_3$ concentration to 1.25 μM IP$_3$ (12.5× background) in a 4 micron segment in mid-dendrite (Fig. 2). IP$_3$ then spread gradually along the dendrite, providing a permissive effect for Ca^{2+} activation of the IP$_3$ receptors (IP$_3$Rs). Activation of IP$_3$Rs permitted release of Ca^{2+} from the endoplasmic reticulum (ER) stores into the cytosol (Fig. 2a). The elevation in cytosolic Ca^{2+} was mirrored by a depression in ER Ca^{2+} as the wave passed (Fig. 2b). The cytosolic Ca^{2+} wave started once adequate Ca^{2+} had built up to spillover and activate neighboring IP$_3$Rs and initiate sustained positive feedback of Ca^{2+} induced-Ca^{2+}-release (CICR). The wave then spread bidirectionally, as Ca^{2+} and IP$_3$ simultaneously diffused laterally. Ca^{2+} waves were not able to reverse direction and propagate back towards their source due to an IP$_3$R refractory period provided by inactivation gating. Parameters including d_{IP_3} (1.415 μm^2/ms),

$d_{\text{Ca}^{2+}_{\text{cyt}}}$ (0.08 μm^2/ms), $d_{\text{Ca}^{2+}_{\text{ER}}}$ (0.08 μm^2/ms), $\bar{p}_{\text{IP}_3\text{R}}$ (120400.0 molecules/mM/ms), $\bar{p}_{serca}$ (1.9565 molecules/ms), and $\bar{p}_{leakER}$ (18.06 molecules/mM/ms) were adjusted from modeling (Wagner et al., 2004) and experiments (Allbritton et al., 1992), to produce a wave speed of 77 μm/s, which is comparable to neuronal Ca^{2+} wave speeds measured experimentally (68±22 μm/s in Nakamura et al. (1999)). These parameters provided our baseline simulation for further parameter explorations. Median Ca^{2+} elevation lasted ~ 1 s and peaked at 1.6 μM, both also comparable with experimental results (Ross et al., 2005; Fitzpatrick et al., 2009).

3.1 IP$_3$R density modulates excitability

IP$_3$R was necessary for wave generation (Fig. 3). Ca^{2+} waves did not begin below IP$_3$R density of 92.2% of baseline, when the first wave was obtained (Fig. 3a and left red dots on c,d,e,f). This wave had initiation delays ~100 ms longer compared to the baseline wave (Fig. 2a and middle red dot on Fig. 3c), with only a slightly lowered amplitude, lower speed, and lower duration. The major effect, time to onset, was strongly dependent on IP$_3$R due to the need to gradually source a sufficient amount of Ca^{2+} to produce enough lateral spillover to initiate a positive feedback cycle, as the lower IP$_3$R density produced a lower total Ca^{2+} flux from ER to cytosol. ER Ca^{2+} must also be sourced at a rate that exceeds the reuptake

governed by SERCA pumping. With increased density, time to onset decreased rapidly to a low of 25 ms.

Speed increased proportionately with increased IP_3R (Fig. 3d). At the lowest value, wave speed was 72 μm/s. Speed depended on both the rate of ER sourcing at each point of wave regeneration, and the rate of diffusion required to reach the next set of IP_3Rs laterally. Proportionate increase in speed with density was due to the reduced requirement for additional Ca^{2+} for positive feedback, since less Ca^{2+} is needed to trigger the release of Ca^{2+}. At each location, IP_3R must source adequate Ca^{2+} not only for positive feedback and spillover, but also to exceed the local sink back into ER provided by the SERCA pump. Ca^{2+} wave duration and amplitude both had a small positive association with increases in IP_3R (Fig. 3e,f), due to the higher density of IP_3Rs liberating more Ca^{2+} for the wave, which then remained elevated longer.

3.2 SERCA opposes IP₃R effects

The SERCA pump returns Ca^{2+} back into the ER, opposing the release from IP_3R conductance. Therefore, the parameter dependence of measures was generally opposite to that seen with IP_3R density (Fig. 4). The least excitable wave was produced at the highest SERCA density tested (Fig. 4b). The most excitable wave shown here, at 0.66× baseline SERCA (Fig. 4a), was caused by diminished Ca^{2+} reuptake after release. Further reduction in SERCA resulted first in spontaneous Ca^{2+} waves and then in simultaneous release from all ER sites at once due to regenerative responses starting from baseline levels (not shown).

Patterns of wave measures were similar to, but reversed from, those seen with IP_3R increase. Onset to the first wave varied from 30 to 330 ms. Shorter onset times were produced by faster Ca^{2+} accumulation with less reuptake. Similarly, the most excitable wave had a faster propagation speed (84 μm/s) and longer duration due to longer-lasting Ca^{2+} supporting faster spread. Amplitude showed a slight inverse relationship with increasing SERCA density, due to the higher SERCA reuptake of Ca^{2+} into ER stores diminishing Ca^{2+} availability for the wave (Fig. 4f).

At the maximal SERCA consistent with wave propagation, 1.07× baseline, onset to wave initiation was increased dramatically (330 ms), wave speed decreased to ~75 μm/s, and duration decreased to 0.82 s (Fig. 4b). Ca^{2+} waves were no longer able to initiate at higher levels, as Ca^{2+} was sucked back into the ER before a Ca^{2+} wave could ignite.

3.3 IP₃R / SERCA balance regulates wave induction

The balance between IP_3R and SERCA density determined whether Ca^{2+} waves could be elicited via IP_3 stimulation (Fig. 5). Excessive Ca^{2+} or insufficient IP_3R would not allow a wave (regions 1,4). Maximum Ca^{2+} level in region 1 was low compared to regions 2 and 3, since ER Ca^{2+} had already partially leaked out of the ER prior to the IP_3 stimulus, and then diffused within the dendrite, preventing the large, localized rise in cytosolic Ca^{2+} which formed a Ca^{2+} wave.

Moving from region 1 towards region 2, IP_3R density decreased and SERCA density increased, both of which reduced cytosolic Ca^{2+}, which was no longer sustained above

threshold throughout the simulation. This allowed the IP_3 stimulus to elicit distinct waves. However, the high levels of IP_3R produced multiple waves without return to a subthreshold state. These repetitive waves caused an artifactual lowering of measured wave speed (see Methods for details of calculation). Ca^{2+} amplitude was higher than in region 1 due to repeated higher elevations of cytosolic Ca^{2+} compared to balanced fluxes in region 1.

In region 3, there was a match across IP_3R and SERCA density, allowing for a single wave to be elicited from the IP_3 stimulus. Within this region, for any given SERCA density, an increase in IP_3 density increased Ca^{2+} flux from ER to cytosol, reducing time to onset, and increasing speed, duration, and amplitude. In region 4, SERCA dominated the dynamics, shuttling Ca^{2+} back into the ER too quickly to allow IP_3 stimulation to initiate a Ca^{2+} wave.

3.4 IP_3 diffusibility regulates wave onset and speed

Altering the IP_3 diffusion constant (d_{IP3}) had a pronounced effect on Ca^{2+} wave initiation (Fig. 6). With low d_{IP3} (0.1415 μm^2/ms), the IP_3 stimulus remained localized in the central stimulus region (~500 μm), producing a high prolonged local elevation with more rapid activation of local IP_3Rs and shorter wave onset time (40 ms). Ca^{2+} near the stimulus then remained elevated longer than at other dendritic locations. Since the IP_3 stimulus spread to neighboring dendritic locations more slowly, Ca^{2+} wave speed was slightly reduced (73.5 μm/s).

High d_{IP3} (1.981 μm^2/ms) significantly delayed the onset of the Ca^{2+} wave (230 ms; Fig. 6b), due to IP_3 diffusing quickly away, producing less local IP_3R stimulation and increasing the time required to trigger the wave. However, once the wave was initiated, it spread slightly faster (77.6 μm/s), the pre-arriving IP_3 giving a slight boost at subsequent locations along the dendrite. Amplitude had a minimal inverse relationship with increasing d_{IP3} (Fig. 6f) because local IP_3 spread out more quickly, reducing local IP_3R activation. At d_{IP3} values larger than 1.981 μm^2/ms, IP_3 was so diffuse, that it could not elicit the Ca^{2+} wave.

Overall, increasing d_{IP3} caused delayed onet (Fig. 6c), a minor increase in speed (Fig. 6d), and no appreciable change in duration or amplitude (Fig. 6ef).

3.5 Pseudo-saltatory waves via IP_3R hotspots

The prior simulations were performed using uniform density of ER mechanisms at all locations. However, there is evidence of inhomogeneities, for example at dendritic branch-points, where elevations in local IP_3R density (IP_3R hotspots) might contribute to assisted propagation of Ca^{2+} waves at these sites of potential failure (Fitzpatrick et al., 2009). In neurons, hotspots have average center-to-center spacing of approximately 20 μm (edge-to-edge spacing of 10 μm) but show considerable variability in the spacing (Fitzpatrick et al., 2009). In the following simulations, we varied hotspot IP_3R density while keeping the inter-hotspot IP_3R density at 80% of baseline.

Both IP_3R hotspot strength and spacing altered Ca^{2+} wave speeds (Fig. 7). We started with a 20% reduction in density between hotspots (Fig. 7a), with the hotspots having 93% of the IP_3R density used in Fig. 2. This alteration reduced wave speed from 77 to 68 μm/s. However, the propagation pattern differed qualitatively, with its saltatory nature readily seen

as spots of high Ca^{2+} concentration which occur at the locations of IP_3R hotspots. Local velocity parallels amplitude in showing an increase at the hotspots, where activation produces a local highly varying gradient (peaked high second spatial derivative) leading to a higher immediate diffusion speed. Slower wave progression occurs between hotspots where lower IP_3R concentration only slightly boosts the wave progression from diffusion. Increased IP_3R density at hotspots increased wave speed further to 90 μm/s (2.0× baseline; Fig. 7b). Further augmentation provided an approximately linear increase in speed due to faster and larger release of Ca^{2+} from the ER stores at the hotspots (Fig. 7c). Below ~93% of hotspot IP_3R density, the waves did not initiate, since there was insufficient Ca^{2+} release to trigger waves (0 speeds at left of Fig. 7c). Wave propagation also did not occur in the absence of IP_3R between hotspots, with the threshold for Ca^{2+} wave initiation having inter-hotspot and hotspot IP_3R densities of ~0.66 and ~0.93× baseline, respectively.

Hotspot spacing also modulated Ca^{2+} wave speeds, with larger spacing producing slowing as Ca^{2+} and IP_3 had to travel further via mildly-boosted diffusion between hotspots before being fully rebooted. At 1.87× baseline IP_3R density with a spacing of 15 μm, the wave had a speed of 100 μm/s (Fig. 7d). Increasing center-to-center spacing between hotspots to 100 μm resulted in reduction of wave propagation speed to 66 μm/s. At the densities shown, hotspot spacing had a larger impact on wave speed (~66–100 μm/s) than IP_3R density (~68–90 μm/s).

Intracellular Ca^{2+} concentration is heavily regulated via buffering mechanisms, in part presumed to provide careful regulation of Ca^{2+}-triggered signaling cascades. Ca^{2+} buffering also modulates Ca^{2+} diffusion efficacy and apparent Ca^{2+} diffusion coefficient ($\mathbf{D}_{Ca(App)}$). Because we were not modeling buffering directly in these simulations, we altered $\mathbf{D}_{Ca(App)}$ instead. Changing $\mathbf{D}_{Ca(App)}$ dramatically altered propagation speed over a wide range (Fig. 8). With diminished $\mathbf{D}_{Ca(App)}$, wave speed was substantially reduced to 25 μm/s (Fig. 8a). The converse of this was that Ca^{2+} was relatively immobile, with duration at one location slightly increased (Fig. 8e). This heightened local Ca^{2+} elevation also allowed for a shorter onset to wave initiation (20 ms; Fig. 8c). Increasing $\mathbf{D}_{Ca(App)}$ above baseline level had opposite effects: wave speed was augmented (288 μm/s) but time to onset was delayed (40 ms), both due to faster spread of Ca^{2+}. We also note that while onset varied nearly linearly, speed showed much greater alteration.

3.6 Pseudo-saltatory waves via ER *stacks*

There are at least two ways that hotspots could occur in dendrites: Type 1. increased density of IP_3R at particular locations on homogeneous distribution of ER; Type 2. increased "density" (accumulation) of ER at particular locations. The former case was explored in the prior section. The latter case has been identified as locations of ER lamellar specialization that are sometimes described as ER *stacks*. We next explored such stacks as an alternative type of hotspot, noting that this increase in local ER provides increased density of SERCA and leak as well as IP_3R at the hotspot locations. In these simulations, the ER density between stacks was at 0.8× baseline, consistent with continuous ER throughout the dendrite (Martone et al., 1993; Terasaki et al., 1994).

Increasing ER stack density from ~0.8× (Fig. 9a) to ~2× baseline (Fig. 9b), increased wave speed from 68 μm/s to 86 μm/s (Fig. 9c). This is due to more release of Ca^{2+} from the leak and IP_3R channels, which was opposed by heightened SERCA activity. The duration of Ca^{2+} amplitude elevation was reduced at the ER stacks. In addition, as the ER stack density increased, the onset to wave initiation shortened (220 to 30 ms), due to heightened leak and IP_3R extrusion of Ca^{2+} into cytosol. However, Ca^{2+} elevation duration decreased as the ER stack density increased (965 to 795 ms), due to heightened SERCA pumping.

Increasing the center-to-center spacing of ER stacks, while maintaining a fixed ER density of 1.86× baseline (Fig. 9d–f), tended to decrease wave speed (93 to 71 μm/s). This was due to lower overall availability of ER for releasing Ca^{2+} and spreading the wave. Interestingly, with heightened center-to-center spacing (15 and 100 μm) of ER stacks, the duration of heightened Ca^{2+} elevation was increased (755 to 960 ms), due to lower overall presence of SERCA pumps.

Waves could not initiate below a minimum of 0.8× ER stack density due to insufficient Ca^{2+} sourcing. Effects of density and spacing of stacks were generally similar to those seen with IP_3R hotspots. Onset time depended primarily on ER stack density. Variation of $\mathbf{D}_{Ca(App)}$ with ER stacks (Fig. 10), produced results very similar to those seen with Type 1 hotspots (Fig. 8), except that the effects on time to onset were more pronounced. With ER stacks, the onsets were significantly larger (35–70 ms) compared to those for IP_3R hotspots (20–40 ms). These heightened onset times with ER stacks were due to the higher SERCA activity, which reduces cytosolic Ca^{2+} availability.

3.7 Electrical priming enhances Ca^{2+} waves

Adding electrical dynamics (voltage-gated calcium channels – VGCCs, Na^+ and K^+ channels, AMPA synapses) to the dendrite allowed for a more complex set of interactions (Fig. 11). VGCCs admitted extracellular calcium into the cytosol, which was then taken up into the ER via SERCA pumps. Compared to the prior simulations, this increased ER steady-state calcium concentration (0.03 mM), allowing for larger contributions to Ca^{2+} waves. Cytosolic calcium equilibrated to 65 nM, due to a balance between SERCA uptake and VGCC calcium influx. In these simulations, the background IP_3 level was set to 0 mM to prevent spontaneous oscillations due to ongoing activation of IP_3R. Calcium waves were more localized due to this absence of background IP_3.

Activation by a 2.5 mM IP_3 stimulus at 7 s combined with the higher background cytosolic calcium levels to trigger IP_3Rs to release calcium from the ER. ER calcium efflux then triggered a localized calcium wave (Fig. 11a middle,bottom), which spread approximately 150 μm, consistent with experimental data (Fitzpatrick et al., 2009; Hong and Ross, 2007; Ross et al., 2005). The spreading calcium wave produced electrical effects, by contributing to the opening of calcium-dependent potassium channels, which hyperpolarized the membrane to −77 mV. Once the calcium wave had passed, the voltage recovered to baseline.

Prior AMPAergic stimulation (150 pulses; 25 ms interspike interval; 3000–6750 ms) produced spikes and further supplemented the ER calcium stores via a sequence of electrochemical interactions (Fig. 11b,c top): Ca^{2+} entry through VGCCs augmented

cytosolic Ca^{2+} (early rise of 65–120 nM at center), augmenting ER Ca^{2+} via uptake (Fig. 11b center). This gradually increased Ca^{2+} throughout the dendrite (0.03–0.045 mM at center), *priming* the ER. Subsequent IP_3 activation was then able to liberate more ER calcium, inducing a higher-amplitude (7.5 μM) calcium wave (Fig. 11b,c bottom). The larger amount of calcium liberated allowed the wave to spread 50 μm further, and produced a longer duration (2 s), compared to the wave produced without synaptic priming. The heightened availability of Ca^{2+} also enhanced the electrical effects, producing greater voltage suppression due to activation of the hyperpolarizing Ca^{2+}-dependent potassium channels.

Increasing the number of AMPA stimuli between 0–150 (interspike interval of 25 ms; AMPA activation at 3 s; IP_3 activation at 7 s) produced nearly linear increases in the IP_3-induced calcium wave amplitude (5.5–7.5μM) and duration (1.6–2.0 s) (not shown). Wave speeds tended to decrease slightly (57–63 μm/s). There was no significant impact of AMPA stimulation on the wave onset, which was relatively fast for all simulations, at 5 ms past the IP_3 stimulation. Using increased background IP_3 (0.01 mM) and increasing the number of AMPA stimuli similarly produced higher amplitude, faster Ca^{2+} waves with IP_3 stimulation (not shown).

4 Discussion

We have developed a reaction-diffusion (R×D) model of neuronal Ca^{2+} waves with multiple compartments (ER and cytosol), multiple diffusing species (Ca^{2+} and IP_3), and multiple ER membrane mechanisms (IP_3 receptors, SERCA pumps, and ER leak). IP_3Rs opened in response to a cytosolic Ca^{2+} and IP_3 stimulus, admitting more Ca^{2+} into the cytosol. Ca^{2+} and IP_3 then diffused and bound to neighboring IP_3Rs, triggering further release of Ca^{2+} and initiating the process of Ca^{2+}-induced-Ca^{2+}-release (CICR). The Ca^{2+} waves had properties matching those observed *in vitro* (Ross et al., 2005), including wave speed (~50–90 μm/s), amplitude (2 μM), and duration (~1 s; Fig. 2). We used our model to compare wave propagation in 3 scenarios: continuous IP_3R distribution, IP_3R hotspots, and ER stacks.

Because the cytosolic Ca^{2+} required for CICR depended on a supply from ER stores via the action of IP_3Rs, the Ca^{2+} waves demonstrated primary sensitivity to IP_3R density, such that wave initiation required a minimal level of IP_3R. IP_3R density correlated negatively with onset, and positively with amplitude, speed, and duration of Ca^{2+} waves (Fig. 3). SERCA pumps were responsible for setting the pace of reuptake of cytosolic Ca^{2+} into the ER and had a large impact on the properties of Ca^{2+} waves (Fig. 4). Low SERCA triggered the generation of hyper-excitable and spontaneous waves. High SERCA diminished wave spread and speed, while increasing onset to wave initiation.

We compared two hypothesized mechanisms for saltatory waves: 1. heightened density of IP_3R (IP_3R *hotspots*), and 2. heightened density of ER (ER *stacks*), where ER stacks heighten local leak and SERCA, as well as IP_3R. IP_3R hotspots were more effective in setting the pace of wave propagation and onset, whereas ER stack augmentation of Ca^{2+} waves was less pronounced due to the opposing effects of SERCA (leak and IP_3R increased

excitability, while SERCA decreased excitability). We hypothesize that IP$_3$R hotspots will predominate since they are the more effective mechanism for boosting Ca^{2+} waves.

Intracellular Ca^{2+} concentration is heavily buffered. Although our model did not contain an explicit representation of buffering mechanisms, we used our model to test the effects of alterations in buffering capacity by modulating the apparent Ca^{2+} diffusion constant ($\mathbf{D}_{Ca(App)}$). We found that $\mathbf{D}_{Ca(App)}$ had potent effects on Ca^{2+} wave speed and propagation efficacy. Effects were similar for both IP$_3$R hotspots (Fig. 8) and ER stacks (Fig. 10). Interestingly, at high Ca^{2+} diffusibility, there were competing effects on excitability: higher speed but longer duration to wave initiation (Fig. 8c & d and Fig. 10c & d).

Finally, we extended our chemical signaling model with electrical components, including a set of calcium and voltage-dependent ion channels and synapses. We used this extended model to demonstrate that electrical activation via AMPA synapses and voltage-gated calcium channels primes ER calcium stores, and contributes to enhanced Ca^{2+} waves on subsequent IP$_3$ stimulation (Fig. 11).

4.1 Predictions

Our model allows us to make the following experimentally-testable predictions.

1. Lowering apparent IP$_3$R densities will lead to reduced spread of Ca^{2+} waves. This is testable by using IP$_3$R antagonists (Taylor and Tovey, 2010).

2. Reductions in SERCA with antagonist (*e.g.*, thapsigargin) will lead to hyperexcitability with multiple or spontaneous Ca^{2+} waves.

3. Dendritic branch-point hotspots will be IP$_3$R hotspots rather than ER stacks, allowing optimal boosting at locations where the wave might otherwise fail. Testable by using immunohistochemistry to look for IP$_3$Rs and correlating with electron microscopy evaluation of stacking/ER concentration.

4. Increased buffering with added diffusible buffers provided via whole cell patch will reduce Ca^{2+} wave velocity. This is testable by modulating buffering properties and effectiveness via supply of Mg^{2++} (for parvalbumin modulation), BAPTA (for calbindin modulation), or EGTA (ethylene glycol tetraacetic acid) (Storm, 1987). Additionally, the use of dye indicators, used to follow wave progression, will alter velocity and other wave properties.

4.2 Roles of ER and of Ca^{2+} waves

Since neuronal dendritic trees are very large (hundreds of microns), diffusion alone would make it impossible for dendritic Ca^{2+} to reach presumed targets in the soma and other dendritic locations for use in modulation of physiological processes including: synaptic plasticity, transcription regulation, and membrane current regulation (*e.g., I*$_h$). Our modeling emphasizes that Ca^{2+} waves can have large variability in speed and distance of propagation, which will have major effects on how Ca^{2+} is distributed and which targets are hit at what concentrations. However, we note that an entirely different role for ER has been proposed by Shemer et al. (2008). Instead of a role for ER in enhancing Ca^{2+} waves, they suggested

that the ER forms a "cable-within-a-cable" which is electrically active and would provide more rapid distal to proximal communication via electrical signaling comparable to that of the plasma membrane.

Pathologically, Ca^{2+} dysregulation may occur via multiple pathways, including heightened IP_3R density, lowered SERCA density, or altered buffering. Dysregulation of Ca^{2+} homeostasis has been implicated in Alzheimer's disease (Lytton et al., 2014; Rowan and Neymotin, 2013; Rowan et al., 2014) and in ischemia, where Ca^{2+} signaling is an important element in the triggering of apoptosis (Green and LaFerla, 2008; LaFerla, 2002; Stutzmann, 2005; Thibault et al., 1998; Zündorf and Reiser, 2011; Taxin et al., 2014).

Acknowledgments

References

Allbritton NL, Meyer T, Stryer L. Range of messenger action of calcium ion and inositol 1, 4, 5-trisphosphate. Science. 1992; 258(5089):1812–1815. [PubMed: 1465619]

Berridge M. Neuronal calcium signaling review. Neuron. 1998; 21:13–26. [PubMed: 9697848]

Blackwell K. Approaches and tools for modeling signaling pathways and calcium dynamics in neurons. J Neurosci Methods. 2013 in press.

Busa W, Nuccitelli R. An elevated free cytosolic Ca^{2+} wave follows fertilization in eggs of the frog, Xenopus laevis. The Journal of cell biology. 1985; 100(4):1325. [PubMed: 3980584]

Carnevale, N.; Hines, M. The NEURON Book. New York: Cambridge University Press; 2006.

De Schutter E. Why are computational neuroscience and systems biology so separate? PLoS Comput Biol. 2008; 4(5):e1000078. [PubMed: 18516226]

De Schutter E, Smolen P. Calcium dynamics in large neuronal models. Methods in neuronal modeling: from ions to networks. 1998; 2

De Young G, Keizer J. A single-pool inositol 1, 4, 5-trisphosphate-receptor-based model for agonist-stimulated oscillations in Ca^{2+} concentration. Proceedings of the National Academy of Sciences of the United States of America. 1992; 89(20):9895. [PubMed: 1329108]

Fall C, Rinzel J. An intracellular Ca^{2+} subsystem as a biologically plausible source of intrinsic conditional bistability in a network model of working memory. Journal of Computational Neuroscience. 2006; 20(1):97–107. [PubMed: 16511655]

Fall C, Wagner J, Loew L, Nuccitelli R. Cortically restricted production of ip3 leads to propagation of the fertilization ca2+ wave along the cell surface in a model of the xenopus egg. Journal of theoretical biology. 2004; 231(4):487–496. [PubMed: 15488526]

Fitzpatrick J, Hagenston A, Hertle D, Gipson K, Bertetto-D'Angelo L, Yeckel M. Inositol-1,4,5-trisphosphate receptor-mediated ca2+ waves in pyramidal neuron dendrites propagate through hot spots and cold spots. J Physiol. 2009; 587(7):1439–1459. [PubMed: 19204047]

Fontanilla R, Nuccitelli R. Characterization of the sperm-induced calcium wave in xenopus eggs using confocal microscopy. Biophysical journal. 1998; 75(4):2079–2087. [PubMed: 9746550]

Green K, LaFerla F. Linking calcium to Aβ and Alzheimer's disease. Neuron. 2008; 59(2):190–194. [PubMed: 18667147]

Gunter T, Yule D, Gunter K, Eliseev R, Salter J. Calcium and mitochondria. FEBS letters. 2004; 567(1):96–102. [PubMed: 15165900]

Harris K. Dendritic spines. Wiley Online Library. 1994

Hartsfield, J. PhD thesis. Baylor College of Medicine; 2005. A quantitative study of neuronal calcium signaling.

Hines M, Morse T, Migliore M, Carnevale N, Shepherd G. ModelDB: a database to support computational neuroscience. J Comput Neurosci. 2004; 17(1):7–11. [PubMed: 15218350]

Hong M, Ross W. Priming of intracellular calcium stores in rat ca1 pyramidal neurons. The Journal of Physiology. 2007; 584(1):75. [PubMed: 17690146]

Iftinca M, McKay B, Snutch T, McRory J, Turner R, Zamponi G. Temperature dependence of T-type calcium channel gating. Neuroscience. 2006; 142:1031–1042. [PubMed: 16935432]

Kay A, Wong R. Calcium current activation kinetics in isolated pyramidal neurones of the CA1 region of the mature guinea-pig hippocampus. J Physiol (Lond). 1987; 392:603–616. [PubMed: 2451732]

Kotaleski J, Blackwell K. Modelling the molecular mechanisms of synaptic plasticity using systems biology approaches. Nat Rev Neurosci. 2010; 11(4):239–251. [PubMed: 20300102]

Kretsinger R. Structure and evolution of calcium-modulated proteins. CRC critical reviews in biochemistry. 1980; 8(2):119. [PubMed: 6105043]

LaFerla F. Calcium dyshomeostasis and intracellular signalling in Alzheimer's disease. Nature Rev Neurosci. 2002; 3(11):862–872. [PubMed: 12415294]

Lechleiter J, Girard S, Peralta E, Clapham D. Spiral calcium wave propagation and annihilation in xenopus laevis oocytes. Science. 1991; 252(5002):123. [PubMed: 2011747]

Li Y, Rinzel J. Equations for InsP3 receptor-mediated $[Ca^{2+}]_i$ oscillations derived from a detailed kinetic model: a Hodgkin-Huxley like formalism. Journal of theoretical biology. 1994; 166(4): 461–473. [PubMed: 8176949]

Lipton P. Ischemic cell death in brain neurons. Physiol Rev. 1999; 79(4):1431–1568. [PubMed: 10508238]

Lytton W, Neymotin S, Kerr C. Multiscale modeling for clinical translation in neuropsychiatric disease. J Comput Surgery. 2014; 1(1):7.

Martone M, Zhang Y, Simpliciano V, Carragher B, Ellisman M. Three-dimensional visualization of the smooth endoplasmic reticulum in purkinje cell dendrites. J Neurosci. 1993; 13(11):4636–4646. [PubMed: 8229189]

McCormick D, Huguenard J. A model of the electrophysiological properties of thalamocortical relay neurons. J Neurophysiol. 1992; 68:1384–1400. [PubMed: 1331356]

McDougal R, Hines M, Lytton W. Reaction-diffusion in the NEURON simulator. Front Neuroinform. 2013a; 7:28. [PubMed: 24298253]

McDougal RA, Hines ML, Lytton WW. Water-tight membranes from neuronal morphology files. Journal of neuroscience methods. 2013b; 220(2):167–178. [PubMed: 24091136]

Nakamura T, Barbara J, Nakamura K, Ross W. Synergistic release of Ca2+ from IP3-sensitive stores evoked by synaptic activation of mGluRs paired with backpropagating action potentials. Neuron. 1999; 24(3):727–737. [PubMed: 10595522]

Neymotin S, Hilscher M, Moulin T, Skolnick Y, Lazarewicz M, Lytton W. Ih tunes theta/gamma oscillations and cross-frequency coupling in an in silico CA3 model. PLoS One. 2013; 8:e76285. [PubMed: 24204609]

Neymotin S, McDougal R, Hines M, Lytton W. Calcium regulation of HCN supports persistent activity associated with working memory: a multiscale model of prefrontal cortex. BMC Neuroscience. 2014; 15(Suppl 1):P108.

Orrenius S, Zhivotovsky B, Nicotera P. Regulation of cell death: the calcium–apoptosis link. Nature Reviews Molecular Cell Biology. 2003; 4(7):552–565.

Peercy B. Initiation and propagation of a neuronal intracellular calcium wave. J Comput Neurosci. 2008; 25(2):334–348. [PubMed: 18320300]

Peterson B, Healy M, Nadkarni P, Miller P, Shepherd G. ModelDB: an environment for running and storing computational models and their results applied to neuroscience. J Am Med Inform Assoc. 1996; 3(6):389–398. [PubMed: 8930855]

Pozzo-Miller L, Pivovarova N, Leapman R, Buchanan R, Reese T, Andrews S. Activity-dependent calcium sequestration in dendrites of hippocampal neurons in brain slices. The Journal of neuroscience. 1997; 17(22):8729. [PubMed: 9348342]

Ross WN, Nakamura T, Watanabe S, Larkum M, Lasser-Ross N. Synaptically activated Ca^{2+} release from internal stores in CNS neurons. Cell Mol Neurobiol. 2005; 25(2):283–295. [PubMed: 16047542]

Rowan M, Neymotin S. Synaptic scaling balances learning in a spiking model of neocortex. Springer LNCS. 2013; 7824:20–29.

Rowan M, Neymotin S, Lytton W. Electrostimulation to reduce synaptic scaling driven progression of alzheimer's disease. Front Comput Neurosci. 2014; 8:39. [PubMed: 24765074]

Safiulina VF, Caiati MD, Sivakumaran S, Bisson G, Migliore M, Cherubini E. Control of gaba release at single mossy fiber-ca3 connections in the developing hippocampus. Frontiers in Synaptic Neuroscience. 2010; 2(1) modeldb reference number: 126814.

Shemer I, Brinne B, Tegnér J, Grillner S. Electrotonic Signals along Intracellular Membranes May Interconnect Dendritic Spines and Nucleus. PLoS Computational Biology. 2008; 4(3):e1000036. [PubMed: 18369427]

Spacek J, Harris K. Three-dimensional organization of smooth endoplasmic reticulum in hippocampal ca1 dendrites and dendritic spines of the immature and mature rat. The Journal of neuroscience. 1997; 17(1):190. [PubMed: 8987748]

Stern M. Buffering of calcium in the vicinity of a channel pore. Cell Calcium. 1992; 13(3):183–192. [PubMed: 1315621]

Storm J. Intracellular injection of a ca^{2+} chelator inhibits spike repolarization in hippocampal neurons. Brain Res. 1987; 435(1):387–392. [PubMed: 3123013]

Stutzmann G. Calcium dysregulation, IP3 signaling, and Alzheimers disease. Neuroscientist. 2005; 11(2):110–115. [PubMed: 15746379]

Taxin Z, Neymotin S, Mohan A, Lipton P, Lytton W. Modeling molecular pathways of neuronal ischemia. Prog Mol Biol Transl Sci. 2014; 123:249–275. [PubMed: 24560148]

Taylor C, Tovey S. IP3 receptors: toward understanding their activation. Cold Spring Harb Perspect Biol. 2010; 2(12)

Terasaki M, Slater N, Fein A, Schmidek A, Reese T. Continuous network of endoplasmic reticulum in cerebellar purkinje neurons. Proc Nat Acad Sci. 1994; 91(16):7510–7514. [PubMed: 7519781]

Thibault O, Porter N, Chen K, Blalock E, Kaminker P, Clodfelter G, Brewer L, Landfield P. Calcium dysregulation in neuronal aging and alzheimer's disease: history and new directions. Cell Calcium. 1998; 24(5–6):417–433. [PubMed: 10091010]

Wagner J, Fall CP, Hong F, Sims CE, Allbritton NL, Fontanilla RA, Moraru II, Loew LM, Nuccitelli R. A wave of IP3 production accompanies the fertilization Ca2+ wave in the egg of the frog, Xenopus laevis: theoretical and experimental support. Cell Calcium. 2004; 35(5):433–447. [PubMed: 15003853]

West A, Chen W, Dalva M, Dolmetsch R, Kornhauser J, Shaywitz A, Takasu M, Tao X, Greenberg M. Calcium regulation of neuronal gene expression. Proceedings of the National Academy of Sciences of the United States of America. 2001; 98(20):11024. [PubMed: 11572963]

Winograd M, Destexhe A, Sanchez-Vives M. Hyperpolarization-activated graded persistent activity in the prefrontal cortex. Proc Natl Acad Sci USA. 2008; 105(20):7298–7303. [PubMed: 18474856]

Zündorf G, Reiser G. Calcium dysregulation and homeostasis of neural calcium in the molecular mechanisms of neurodegenerative diseases provide multiple targets for neuroprotection. Antioxid Redox Signal. 2011; 14(7):1275–1288. [PubMed: 20615073]
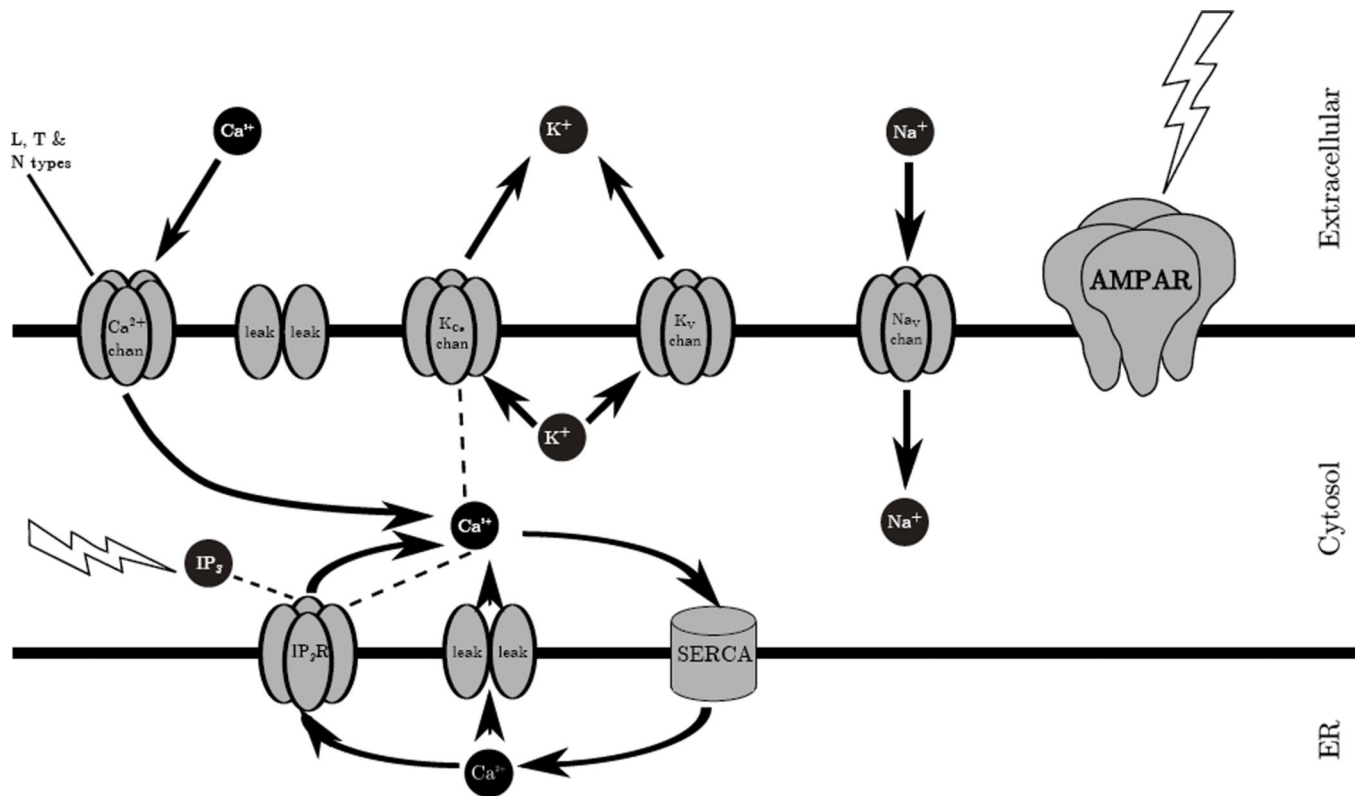
Figure 1.
Schematic of the dendrite model (1000 μm length; 1 μm diameter) showing the extracellular space, cytosol and endoplasmic reticulum (ER). Thick black lines represent the plasma and ER membranes. The extracellular space provides a source and sink for multiple molecules. Ca^{2+}, Na^+, K^+, and IP_3 are depicted as black circles. These molecules enter and exit the dendrite and its sub-compartments via the channels/receptors (gray pores) in directions indicated by arrows. SERCA pump moves cytosolic Ca^{2+} into the ER. Lightning symbols represent stimulus locations (AMPA-mediated depolarization; mGluR-mediated IP_3 augmentation). Dotted lines between molecules and receptors indicate the receptor is modulated by the molecule (*e.g.*, Ca^{2+} activates K_{Ca} and IP_3R).
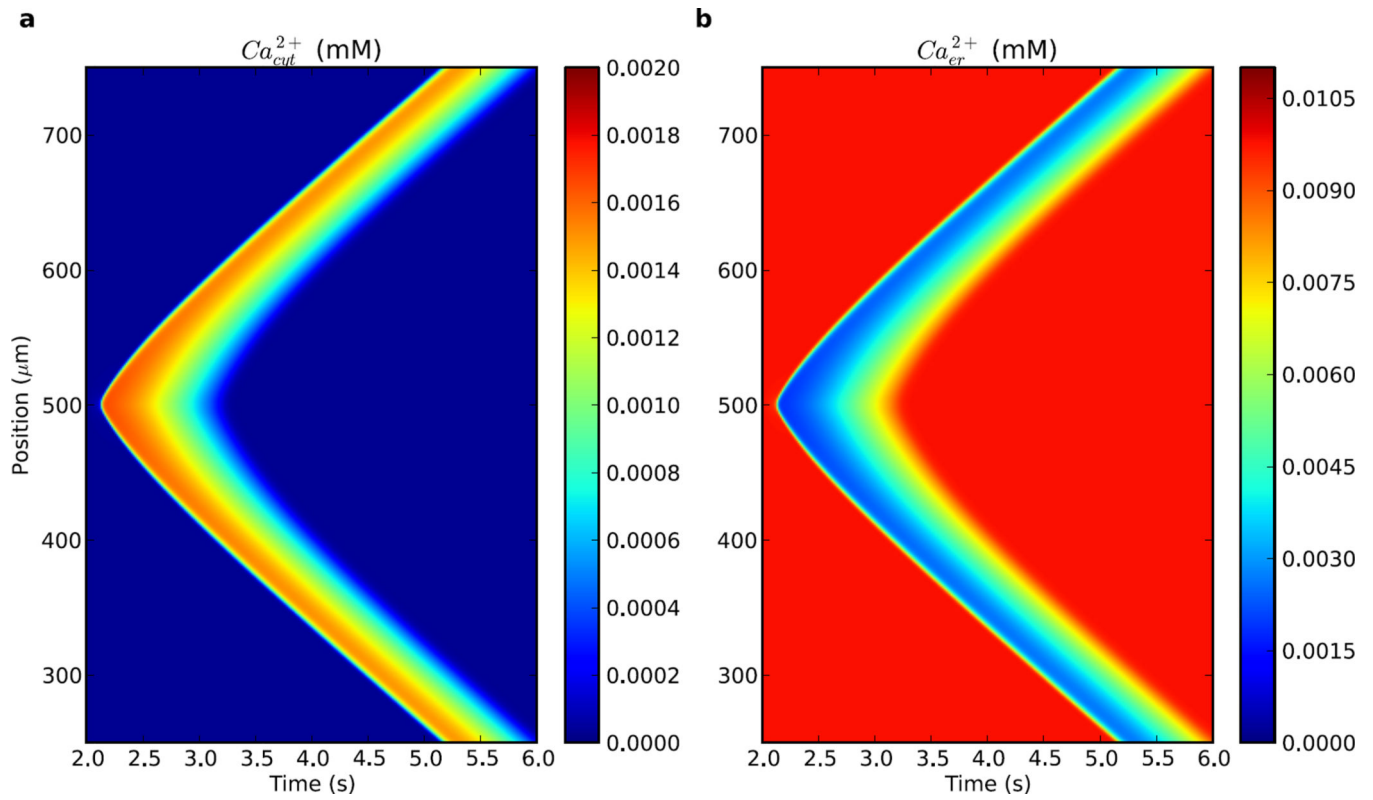
Figure 2.
Ca^{2+} wave propagation with baseline parameters. Elevated IP$_3$ stimulus placed at mid-dendrite (500 μm on y-axis) after 2 s past start of simulation. **(a)** cytosolic [Ca^{2+}] shows a wave of increased concentration **(b)** ER [Ca^{2+}] shows a mirror image wave of decreased concentration as Ca^{2+} is released to cytosol.
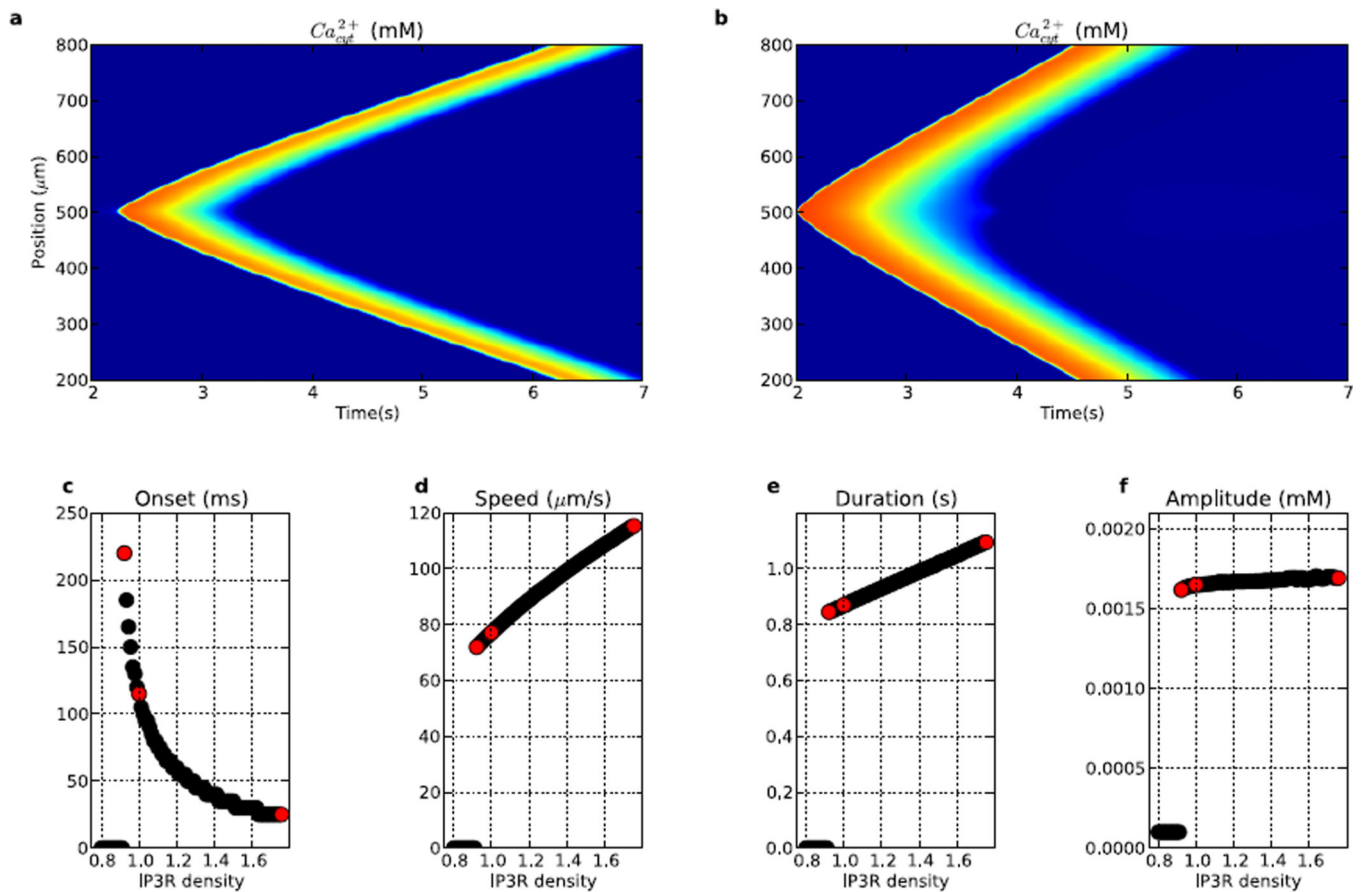
Figure 3.

Ca^{2+} wave propagation is sensitive to the density of IP_3R. From left to right, the three red dots in c–f correspond to features of the following Ca^{2+} waves: **(a)** low IP_3R density (0.9× baseline); baseline IP_3R density (Fig. 2); **(b)** high IP_3R density (1.8× baseline). **(c)** time to wave onset (0 indicates no wave), **(d)** wave propagation speed, **(e)** duration (2× Ca^{2+} elevation; median duration across dendritic locations) **(f)** peak amplitude. (c–f each show 91 different equally spaced parameter values) (Colorscale in **(a)** and **(b)** same as in Fig. 2.)
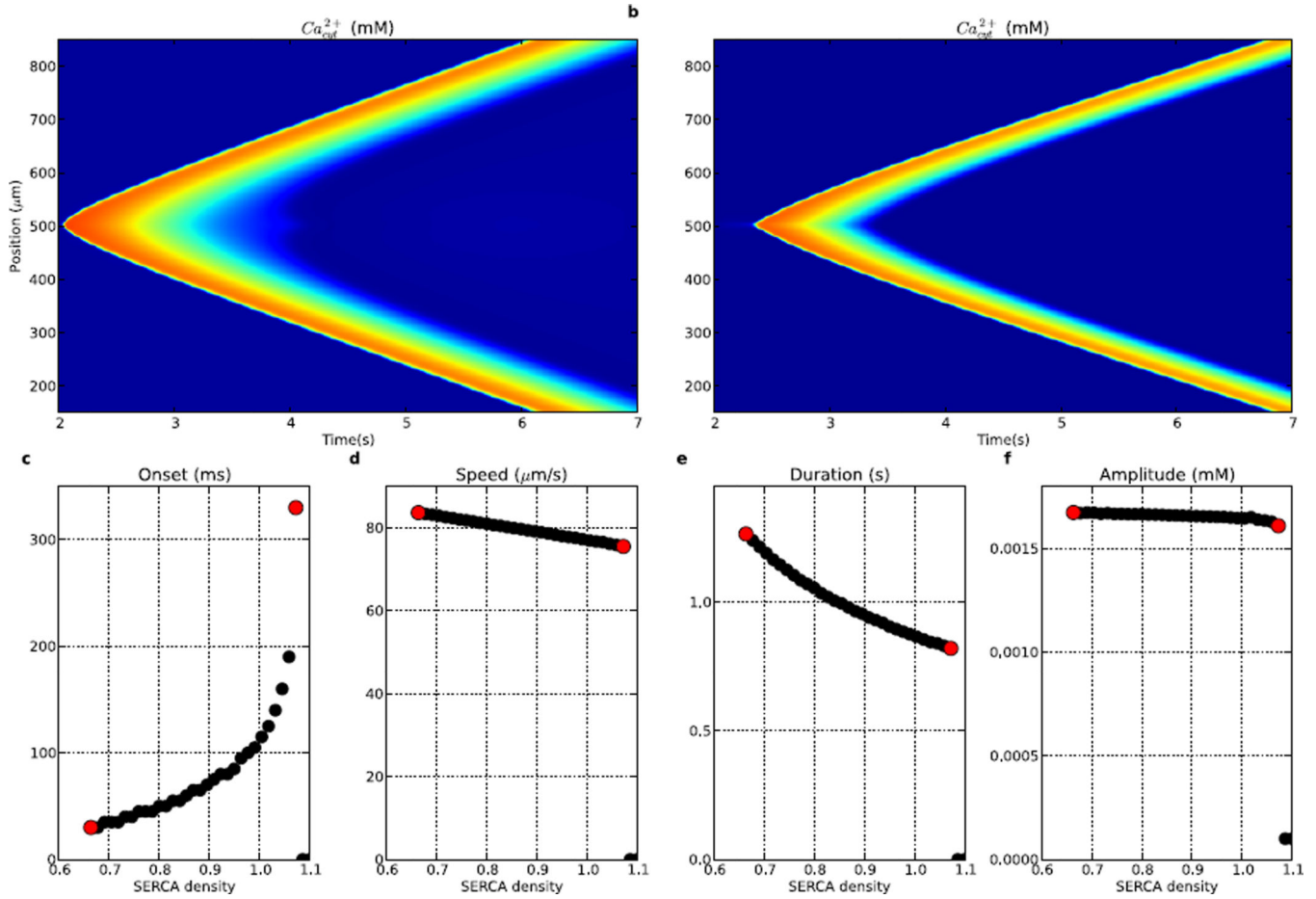
Figure 4.
Ca^{2+} wave propagation is sensitive to the density of SERCA. Tested by varying SERCA density relative to baseline ($n = 45$). **(a)** hyper-excitable Ca^{2+} wave produced with $0.66\times$ baseline SERCA, **(b)** diminished Ca^{2+} wave produced with $1.03\times$ baseline SERCA, **(c)** time to Ca^{2+} wave onset (0 indicates no wave at the SERCA level), **(d)** speed, **(e)** duration (median duration of Ca^{2+} elevation across dendritic locations), **(f)** peak amplitude. Left (right) red dots in c–f corresponds to activity shown in **(a)** (**(b)**). (Colorscale in **(a)** and **(b)** same as in Fig. 2.)
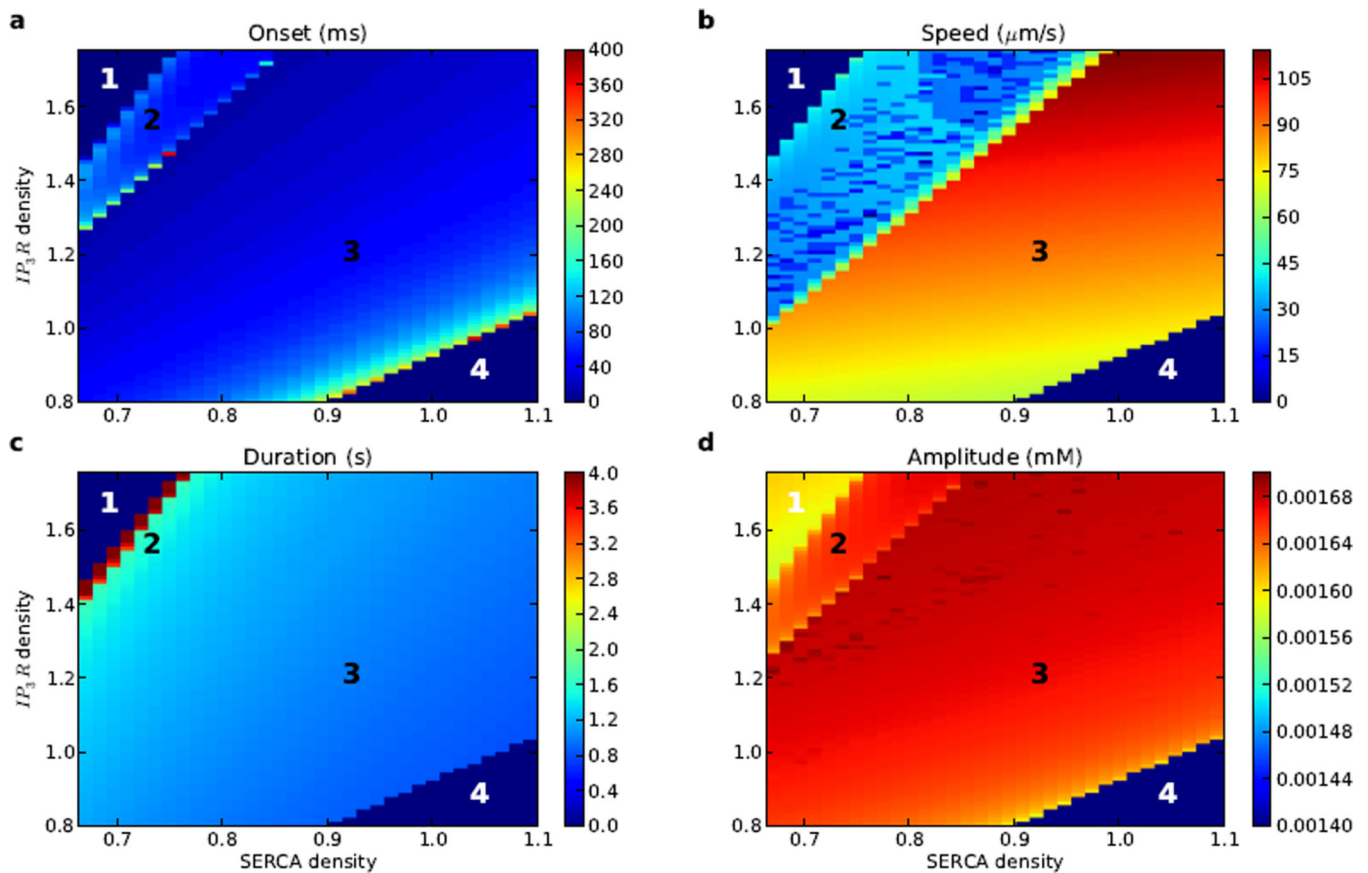
Figure 5.
Ca^{2+} wave propagation is sensitive to density of IP_3R and SERCA. 2838 simulations varying IP_3R (86 levels) and SERCA density (33 levels) relative to baseline shows different dynamics: region 1: sustained Ca^{2+} elevation precluded IP_3-evoked wave; region 2: multiple Ca^{2+} waves; region 3: single Ca^{2+} wave; region 4: insufficient IP_3R to source Ca^{2+} wave. **(a)** time to Ca^{2+} wave onset where present, **(b)** speed where wave present, **(c)** duration where wave present (median duration of Ca^{2+} elevation across dendritic locations), **(d)** maximum calcium level.
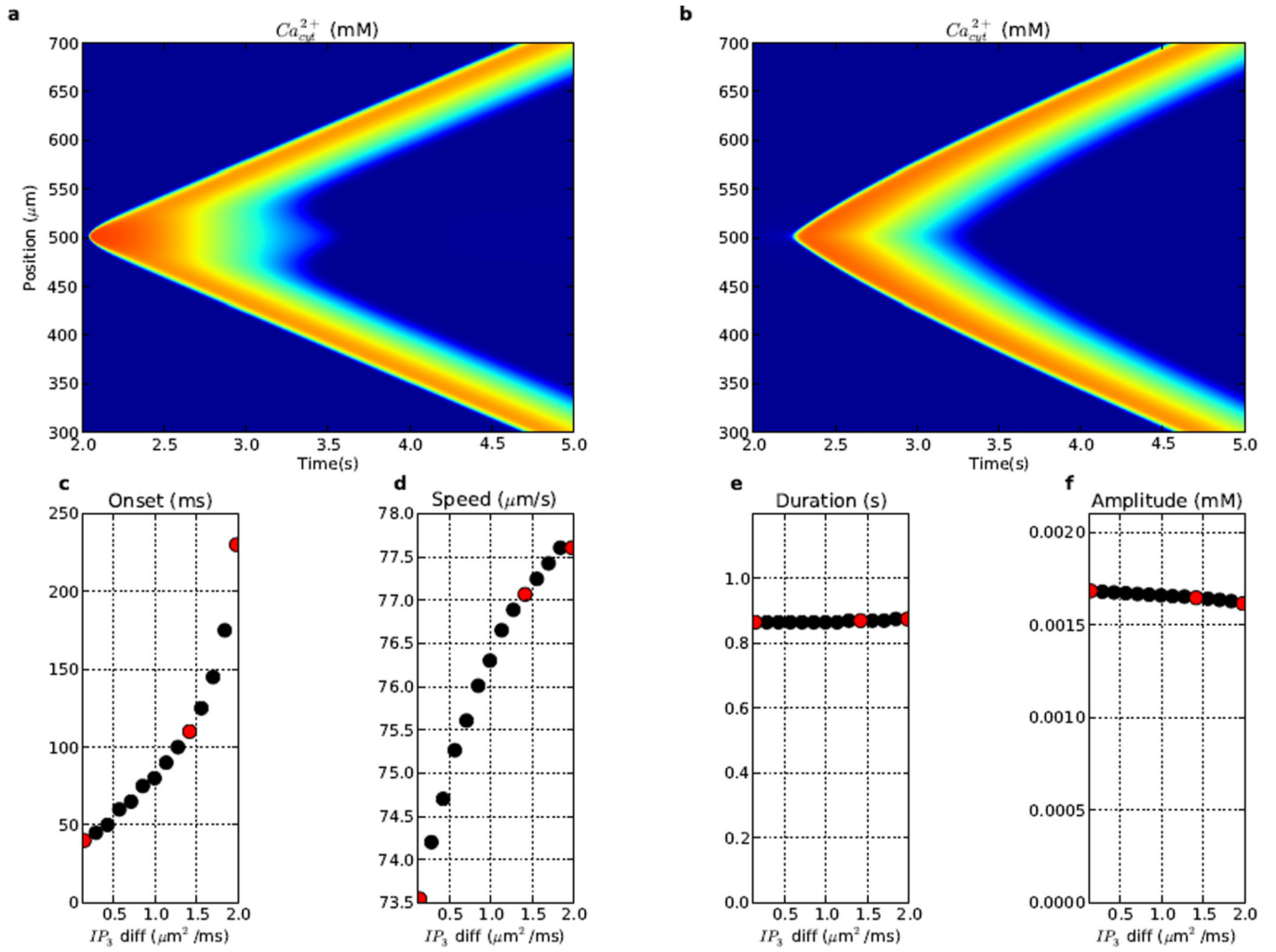
Figure 6.
Ca^{2+} wave propagation is sensitive to IP_3 diffusion coefficient (d_{IP_3}). From left to right, red dots in c–f correspond to features of Ca^{2+} waves with **(a)** low (0.1415 μm²/ms); baseline (1.415 μm²/ms; Fig. 2); **(b)** high (1.981 μm²/ms) d_{IP_3}. **(c)** time to wave onset, **(d)** wave propagation speed, **(e)** duration (2× Ca^{2+} elevation; median duration across dendritic locations) **(f)** peak amplitude. (Colorscale in **(a)** and **(b)** same as in Fig. 2.)
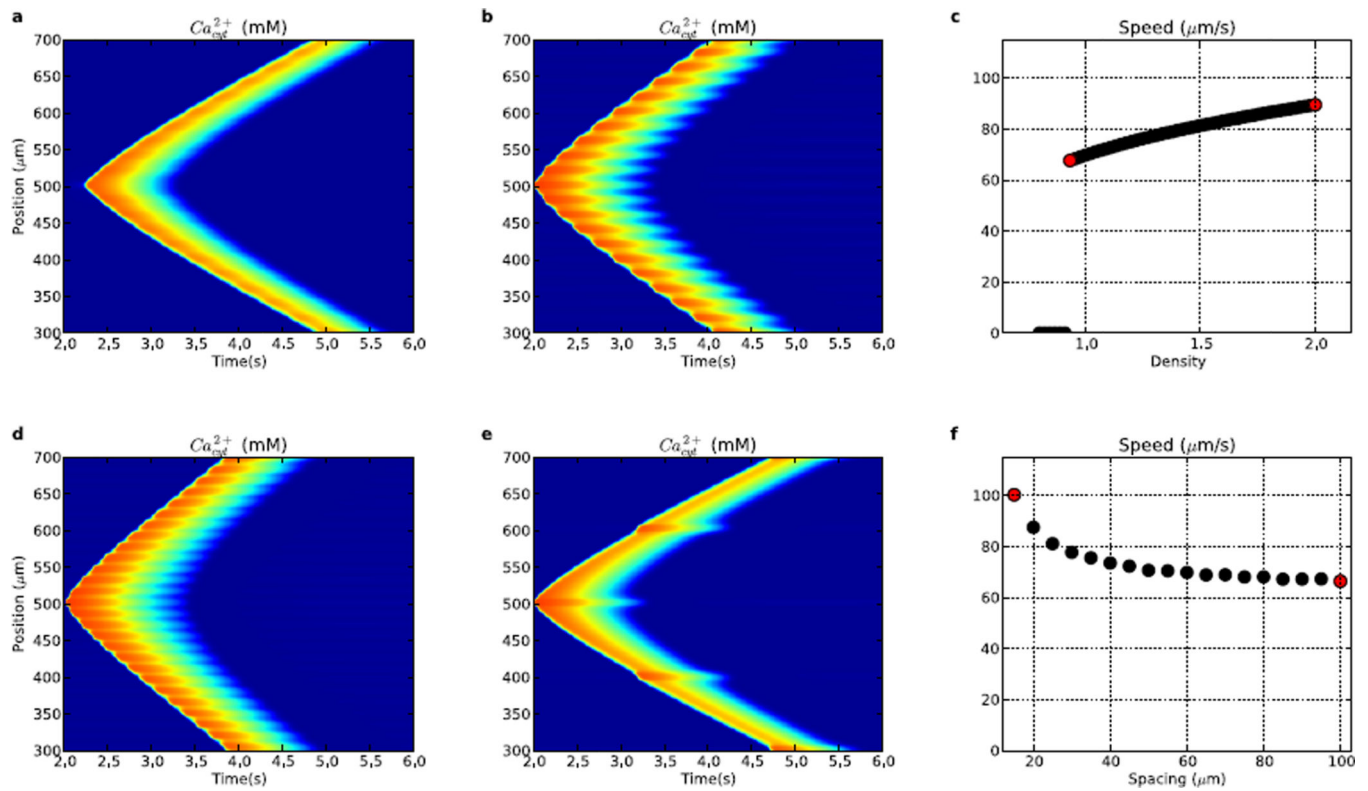
Figure 7.
Comparison of waves (and wave speeds) generated from varying IP$_3$R hotspot density (a–c) and separation (d–f). **(a)** 20 μm spacing; 0.93× density. **(b)** 20 μm spacing; 2× density. **(c)** wave speed as a function of IP$_3$R hotspot density, **(d)** 15 μm spacing; 1.87× density. **(e)** 100 μm spacing; 1.87× density. **(f)** wave speed as a function of IP$_3$R hotspot spacing. (Colorscale in a,b,d,e same as in Fig. 2.) Red points in **(c)** (**(f)**) are from waves in **(a),(b)** (**(d),(e)**).
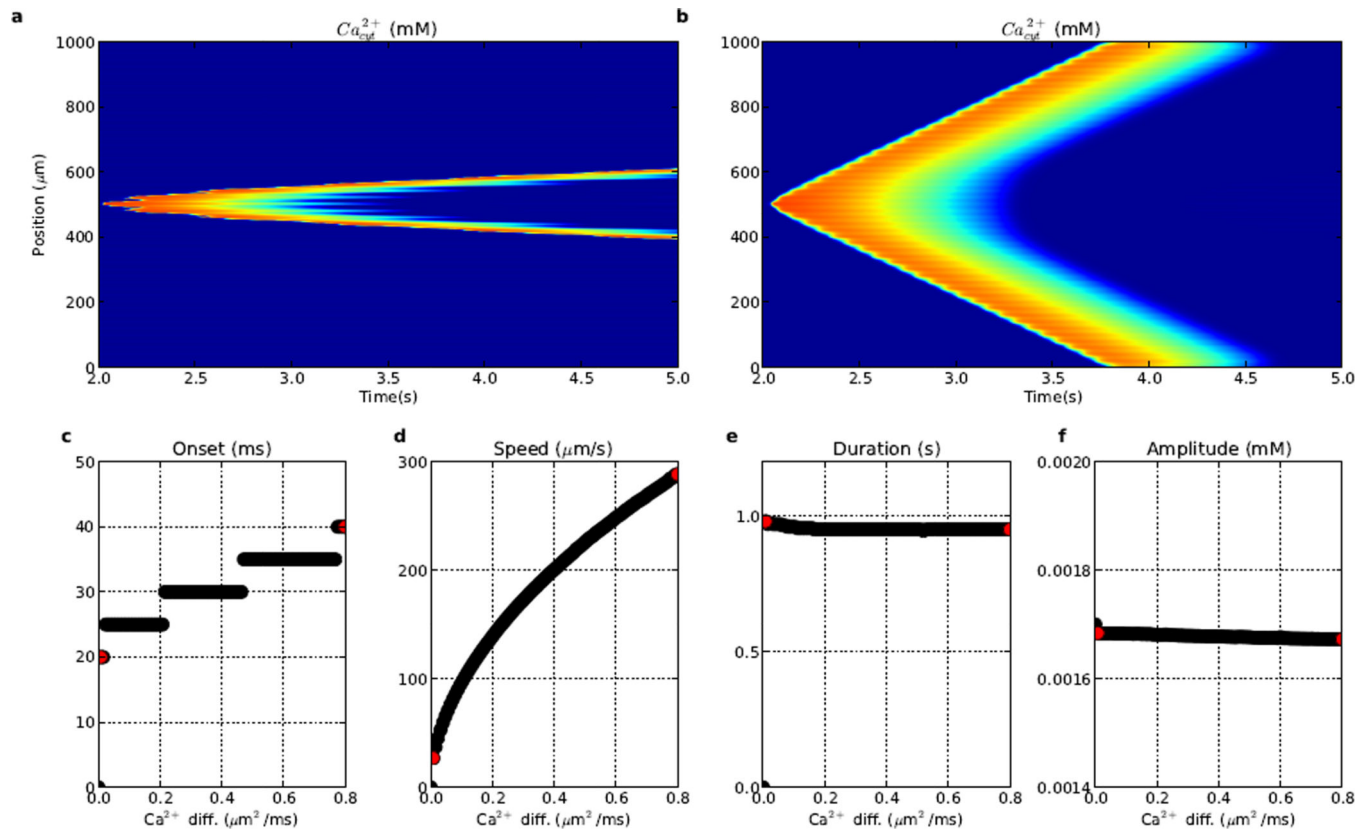
Figure 8.

Comparison of waves generated from varying $\mathbf{D}_{Ca(App)}$ in the presence of IP$_3$R hotspots. Ca^{2+} waves generated when using a Ca^{2+} diffusion coefficient of **(a)** 0.008 μm^2/ms and (b) 0.8 μm^2/ms. **(c)** time to Ca^{2+} wave onset (0 indicates no wave at the Ca^{2+} diffusion level), **(d)** speed, **(e)** duration (median duration of Ca^{2+} elevation across dendritic locations), **(f)** peak amplitude. Left (right) red dots in c–f corresponds to activity shown in **(a)** ((**b**)). (Colorscale in **(a)** and **(b)** same as in Fig. 2.)
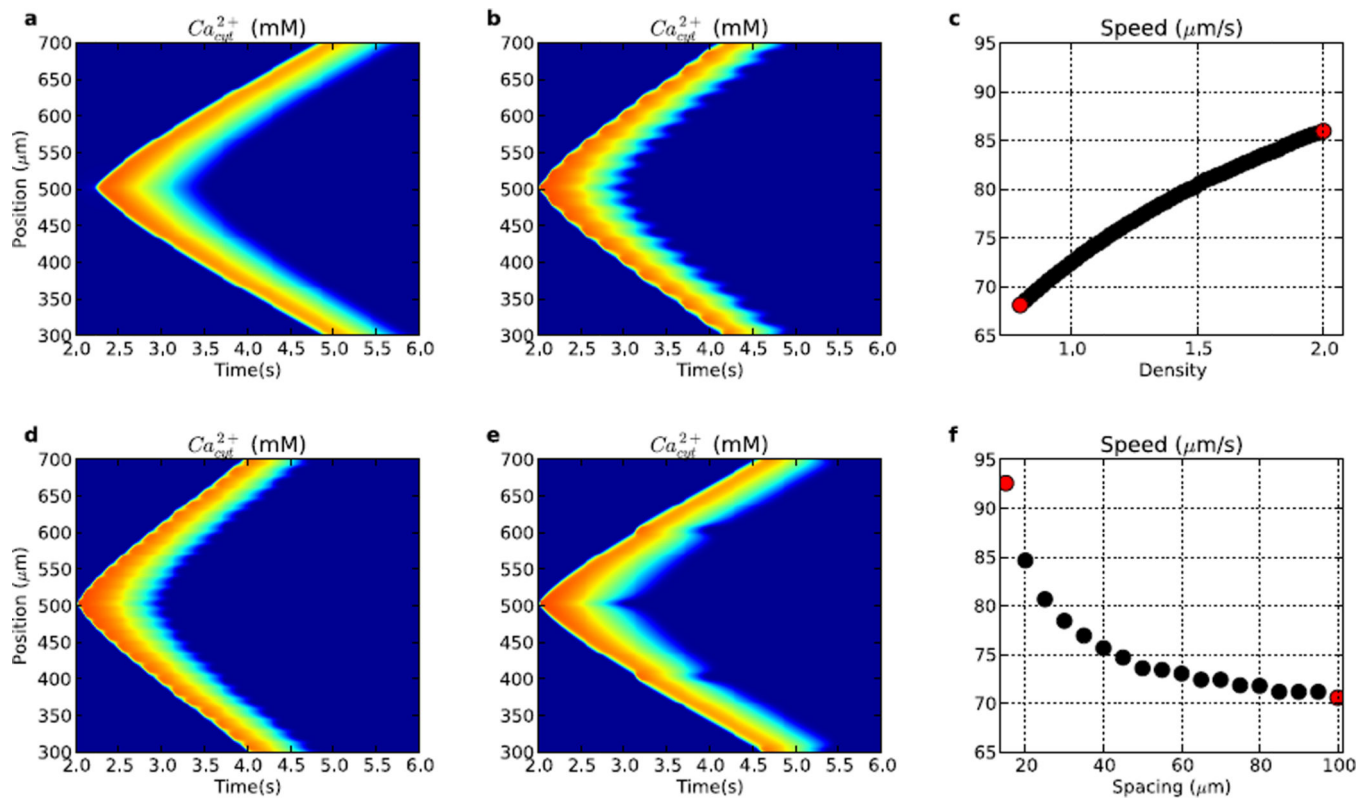
Figure 9.
Comparison of Ca^{2+} waves generated from varying ER stack properties. Simulations were run by varying density and spacing of ER stacks. ER density in between stacks was set at 0.8× baseline. **(a)** Ca^{2+} wave from 0.8× ER stack density with 20 μm spacing, **(b)** Ca^{2+} wave from 2.0× ER stack density with 20 μm spacing, **(c)** Ca^{2+} wave speed as a function of ER stack density (fixed 20 μm spacing), **(d)** Ca^{2+} wave from 15 μm ER stack spacing with ~1.87× density, **(e)** Ca^{2+} wave from 100 μm ER stack spacing with ~1.87× density, and **(f)** wave speed as a function of ER stack spacing. Note the bumps in Ca^{2+} release around ER stacks. (Colorscale in a,b,d,e same as in Fig. 2.) Red points in **(c)** (**(f)**) are from waves in **(a)**, **(b)** (**(d)**,**(e)**).
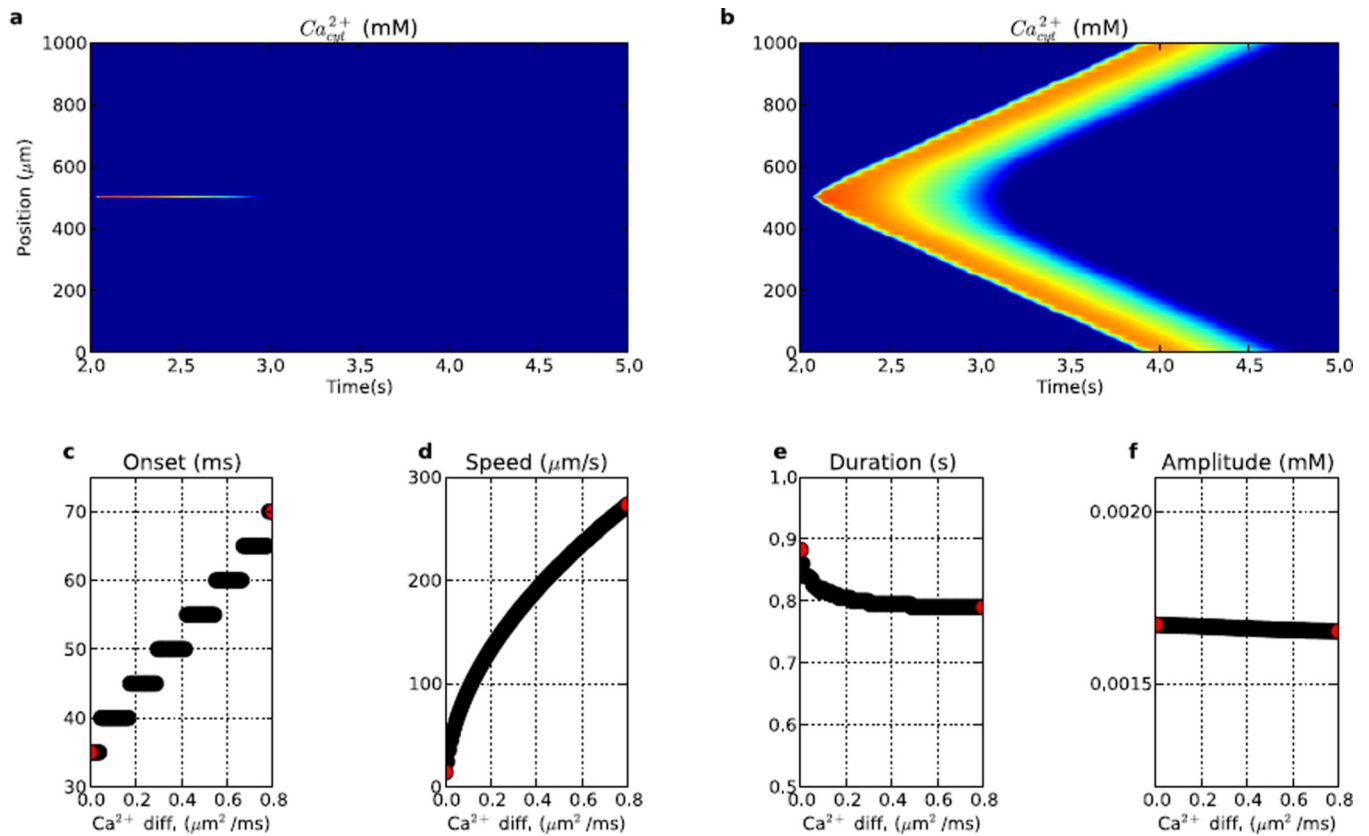
Figure 10.
Comparison of waves generated from varying $\mathbf{D}_{Ca(App)}$ in the presence of ER stacks. **(a)** Local Ca^{2+} event generated with Ca^{2+} diffusion coefficient of 0.0 $\mu m^2/ms$. **(b)** Ca^{2+} waves generated when using a Ca^{2+} diffusion coefficient of 0.8 $\mu m^2/ms$. **(c)** time to Ca^{2+} wave onset, **(d)** speed, **(e)** duration (median duration of Ca^{2+} elevation across dendritic locations), **(f)** peak amplitude. Left (right) red dots in c–f corresponds to activity shown in (a) ((b)). (Colorscale in **(a)** and **(b)** same as in Fig. 2.)
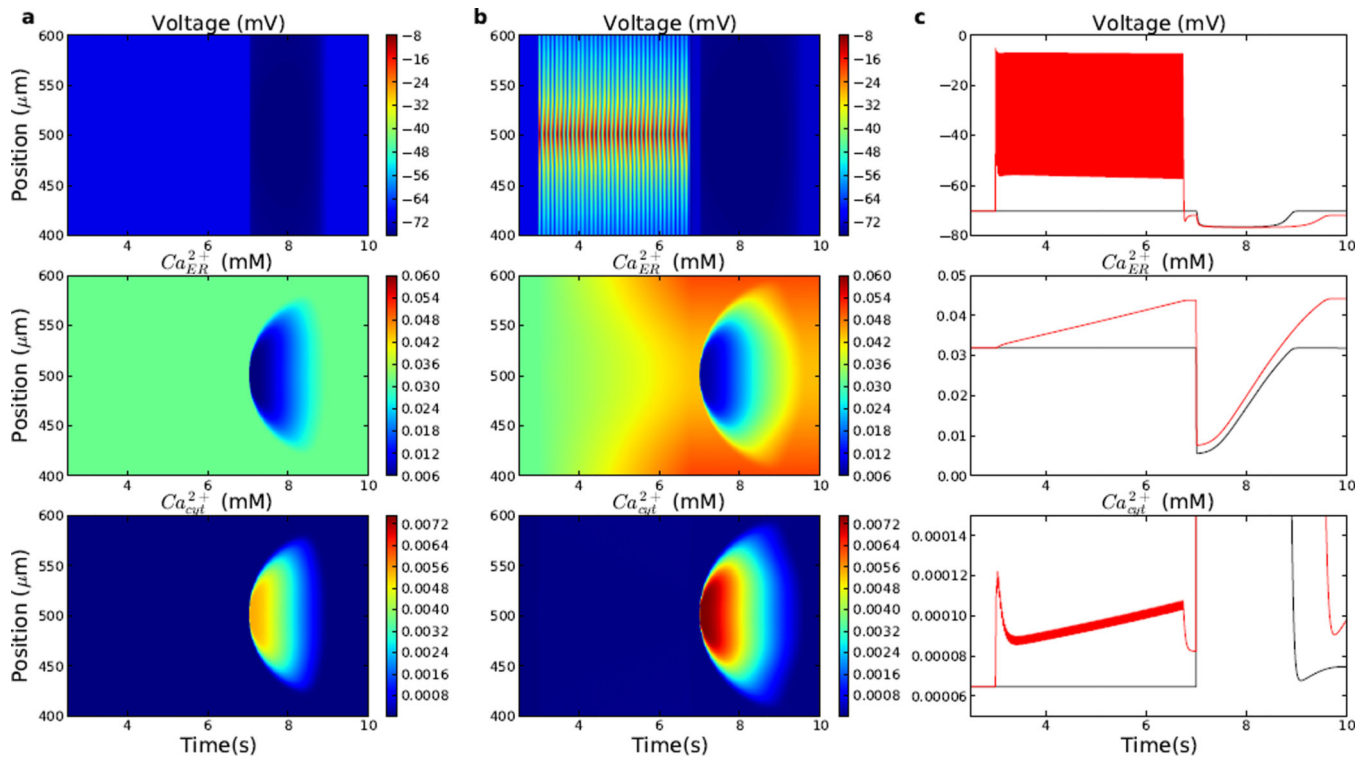
Figure 11.
Electrical stimulation with increased number of AMPA activations enhances Ca^{2+} waves induced by IP_3 (2.5 mM at 7 s). **(a)** Control simulation: Ca^{2+} wave with no AMPA inputs prior to the IP_3 stimulus. **(b)** Ca^{2+} wave with train of 150 AMPA inputs (onset: 3 s; interspike interval: 25 ms) prior to the IP_3 stimulus. **(c)** Comparison of voltage (top), ER Ca^{2+} (middle), and cytosolic Ca^{2+} (bottom) in control (black) and simulation with 150 AMPA inputs (red).

Table 1

Baseline parameters for the Ca^{2+} wave model.

$f_{cyt} = 0.83$

$f_{ER} = 0.17$

$\bar{p}_{IP_3R} = 120400.0$ molecules/mM/ms

$k_{IP_3} = 0.00013$ mM

$k_{act} = 0.0004$ mM

$k_{inh} = 0.0019$ mM

$\bar{p}_{leakER} = 18.06$ molecules/mM/ms

$\bar{p}_{serca} = 1.9565$ molecules/ms

$k_{serca} = 0.0001$ mM

$\tau_{IP_3R} = 400$ ms

$d_{Ca^{2+}_{cyt}} = 0.08 \mu m^2/ms$

$d_{Ca^{2+}_{ER}} = 0.08 \mu m^2/ms$

$d_{IP_3} = 1.415 \ \mu m^2/ms$